J. Fluid Mech. (1999), *vol.* 393, *pp.* 257–308. Printed in the United Kingdom

Direct numerical simulations of turbulence with confinement and rotation

By F. S. GODEFERD† AND L. LOLLINI

École Centrale de Lyon, Laboratoire de Mécanique des Fluides et d'Acoustique, UMR 5509, France

(Received 20 January 1998 and in revised form 22 November 1998)

The goal of this work is to analyse how solid body rotation affects forced turbulence enclosed within solid boundaries, and to compare it to results of the experiment performed by Hopfinger *et al.* (1982). In order to identify various mechanisms associated with rotation, confinement, and forcing, a numerical pseudo-spectral code is used for performing direct numerical simulations. The geometry is simplified with respect to the experimental one. First, we are able to reproduce the linear regime, as propagating inertial waves that undergo reflections at the walls. Second, the Ekman pumping phenomenon, proportional to the rotation rate, is identified in freely decaying turbulence, for which the evolution of the flow bounded by walls is compared to the evolution of unbounded homogeneous turbulence. Finally we introduce a local forcing on a plane in physical space, for simulating the effect of an oscillating grid, so that diffusive turbulence is created, and we examine the structuring of the flow under the combination of the linear and nonlinear mechanisms. A transition to an almost two-dimensional state is shown to occur between the region close to the forcing and an outer region in which vortices appear, the number of which depends on the Reynolds and Rossby numbers. In this region, the anisotropy of turbulence is examined, and the numerical predictions are shown to reproduce many of the most important features present in the experimental flow.

1. Introduction

Solid body rotation considerably affects the dynamics and structure of turbulent flows, partly by selection of three-dimensional instabilities that can occur within them. Generally speaking, the energy transfer from the large scales of turbulence to the small ones is reduced, and in parallel, the flow tends to become two-dimensional. This can lead to a selection, by the rotation effect, of a given range of privileged scales of turbulence. For instance in the atmospheric boundary layer, patterns revealed by the shape of clouds, seen from the Earth, do not show any particular effect of rotation; namely, an observer down on the Earth only perceives small scales of the atmospheric boundary layer. On the other hand, a satellite picture permits observation of the corresponding large-scale flow whose dynamics is essentially driven by the Coriolis force associated with the Earth's rotation (see figure 1 that shows the dominance of cyclonic organized large-scale structures).

The input of energy in such flows, through localized forcing in physical space, can produce a kind of turbulence called diffusive, i.e. with no mean flow, which is also

† Author to whom correspondence should be addressed: e-mail: godeferd@mecaflu.ec-lyon.fr.

FIGURE 1. Cyclonic activity over the North Atlantic Ocean area in 1995. The four cyclones were christened Humberto, Iris, Karen and Luis (Source Météo-France).

thought to play a crucial role in the formation of vortices, and therefore relevant to explaining some features of the atmospheric boundary layer. In addition, diffusive turbulence present in geophysical flows is most important in mixing processes. At small scales, it is responsible for the quasi-homogeneity of the density field in the upper oceanic layer whose thickness is of the order of tens of metres, above the thermocline interface. It acts through the breaking of surface or internal gravity waves that lie at the level of the thermocline. At larger scales, Hopfinger & van Heijst (1993), propose modelling the formation of cyclones in the atmosphere as diffusive turbulence undergoing the rotation effect. Their reasoning, is as follows: let us consider a convective layer; the turbulent flux it generates is turned into a slow descending anti-cyclonic motion; when reaching the ground, the fluid is deflected and a part of it goes, in the shape of more intense cyclones, up to the turbulent layer; the resulting three-dimensional layer should have a given thickness such that the upward moving fluxes can, in turn, be transformed into descending ones, and so on. The experiment by Hopfinger, Browand & Gagne (1982, hereafter referred to as HBG) is a model of the convective layer, by an oscillating grid, the floor being associated with the upper tank lid. As a confirmation, these authors do observe intense cyclones.

As in many complex problems, understanding the action of rotation can be helped by the study of isolated phenomena, as we propose to do in this paper for the inertial waves, Ekman pumping due to the presence of solid boundaries, and the effect of a local forcing. We present here a study based on direct numerical simulations, that illuminate these various isolated effects of rotation on the fluid motion. One of the main goals of this work is to reproduce the context of the experiment by HBG, where the simultaneous action of rotation, confinement and local forcing lead to the appearance of persistent vortex structures, with axes parallel to the rotation one. This behaviour constitutes a fundamental difference with numerical studies of homogeneous rotating turbulence (Bardina, Ferziger & Rogallo 1985; Cambon, Mansour & Godeferd 1997), where the anisotropy develops clearly as a two-dimensionalization of the flow, but without the emergence of clear organized vortices. The study by Cambon *et al.* (1997) has shown the two-dimensionalization tendency of rotating turbulence, but also that the departure of homogeneous turbulence from

isotropy is triggered by nonlinearities, although the latter alone cannot explain the formation of organized structures. It seems that the appearance of such structures is favoured by the presence of solid boundaries through the Ekman pumping mechanism, and the limitation of the length scales in the direction of the rotation axis. The Reynolds stress tensor anisotropy, in the homogeneous case, shows that vertical motion is still present, and that rotation mainly affects the integral length scales, in directions either parallel or perpendicular to the rotation axis. Accordingly, these quantities will in particular be detailed in our study. Following these works on homogeneous turbulence, new problems therefore arise in the inhomogeneous case, such as how the flow reacts to the adverse blocking effect of the walls, and the Ekman pumping phenomenon.

Apart from the simulation of the experiment by HBG, we shall thus isolate the Ekman pumping effect by simulations of freely decaying turbulence, by comparing the different behaviours obtained in the homogeneous – without walls – and inhomogeneous – with walls – cases.

The influence of solid body rotation on flows involves a combination of linear and nonlinear effects. When the Rossby number is much smaller than one, the linear Coriolis term is dominant over the nonlinear and sometimes unsteady terms. Linear effects include the famous Taylor columns (Taylor 1921), and the inertial waves (McEwan 1970). The latter are dispersive, dissipative and anisotropic waves, that transport energy in given directions, depending on the background rotation rate. They have been extensively described by Greenspan (1968), and Phillips (1963), shows their original properties when they reflect on solid boundaries, such as the transfer of energy between wavenumbers and the dissipation of energy.

Simplified analyses can be performed, in order to explain some effects of rotation. One of these involves the Taylor–Proudman theorem for rotating flows, useful in specific circumstances only: it applies to two-dimensional steady flows, where a given external time scale can be identified (such as a towed obstacle in the experiment by Taylor 1921). It has been used to explain somehow the two-dimensionalization of turbulence under the effect of rotation, but it is merely a linear argument that cannot account for the nonlinear transition of initially isotropic homogeneous rotating turbulence (Cambon *et al.* 1997). A subject of debate in the scientific community is the condition for application of the theorem of Taylor–Proudman for strong rotation and the universality of the conclusions drawn. Using the Taylor–Proudman theorem, one can show that those inertial waves (linear mode) that are stationary, necessarily have horizontal wavevectors, representing exactly the two-dimensional mode. Complete two-dimensionalization of course requires $\partial/\partial x = 0$, when rotation is applied on the x-axis, and in the following work we will refer only to two-dimensionalization *trends* – $\partial/\partial x$ comparatively small in a wide part of the flow – without actually achieving an exactly two-dimensional state. The presence of walls in the confined forced simulations, by adding extra dissipation to the inertial waves, and our local forcing, renders the two-dimensionalization mechanisms more complex than within the sole scope of the Taylor–Proudman theorem. This very partial two-dimensionalization is also reflected in the lack of observation of an inverse cascade in our simulations, contrarily to what was observed in previous works dealing with rotating homogeneous turbulence with spectral local forcing (Hossain 1996).

Another, not unrelated, simplified approach is the geostrophic approximation, frequently used in the framework of geophysical flows, and obtained following restrictive approximations. This method models the flow, subjected to gravity and rotation, as a superposition of thin layers within which the density variations are small. The

Reynolds number is assumed to be large and the Rossby number to be small, so that the rotation effect can be included entirely within the horizontal pressure gradient terms. This de-coupling of the horizontal and vertical motion allows one to obtain explicitly the (horizontal) *geostrophic* velocity. Turbulence is said to be quasi-geostrophic when its state is strongly two-dimensional, and the pressure is the hydrostatic equilibrium (Colin de Verdières 1980). This approximation contains the same Rossby and Reynolds numbers conditions as the geostrophic approximation, as well as the thin layers one. A quasi-geostrophic approximation is useful to get the time evolution of the pressure and velocity fields (Pedloski 1986).

The connection of the geostrophic model to a solid boundary, e.g. the ground, through a non-slip boundary condition creates an Ekman layer in which viscous forces and the Coriolis force are in equilibrium. Its thickness is estimated as $\delta = \sqrt{\nu/\Omega}$, and the Ekman number can be defined as $E = (\delta/L)^2$ where L is a macroscopic length scale inside the rotation flow. The Ekman pumping phenomenon comes from the geostrophic equilibrium of a rotating structure connected to the wall, such that a vertical component of the velocity is created from the pressure variation inside the vortex. Depending on the sign of vorticity inside the vortex, it can be either an upward or downward component. Cyclones are for instance shown to lead to upwelling when connected to a bottom boundary, and fluid particle trajectories become helical.

Our paper is organized as follows. Section 2 is devoted to recalling the Navier–Stokes equations in a rotating frame, and some properties of the Coriolis force are enumerated, including results of linear stability analyses and of nonlinear homogeneous approaches. We shall describe the numerical method in § 3. We have adapted a code initially written for the simulation of turbulent channel flows, by Pascal & Buffat (1996). It solves the instantaneous Navier–Stokes equations for an incompressible viscous flow between two parallel infinitely extending walls. The direct numerical simulation (DNS) code uses a pseudo-spectral method built around the decomposition of the fields in Fourier modes in the two periodic (infinite) directions, and Chebyshev modes in the homogeneous direction (normal to the walls). We shall also present definitions of the statistical quantities. In the following sections, we shall present applications of the numerical method to flows in order of increasing complexity, in terms of physical phenomena.

In § 4, the pure linear effect of rotation, through the formation of inertial waves, is studied by numerical simulations. We check that the energy propagation is in agreement with linear theory for the dispersion relation of inertial waves, which will be an assessment of the validity of our numerical approach, at least for the linear and rotation terms. We shall compare the results of our simulations with experimental ones by McEwan (1970).

Section 5 will be devoted to simulations of freely decaying turbulence, both in the homogeneous and inhomogeneous cases, and will focus on the role of rotation and walls, the latter generating the Ekman pumping effect. Anisotropy and the presence of vortex structures will be discussed. The walls will be shown to play an important role in the formation of organized structures, which do not appear in the homogeneous context.

Finally, § 6 deals with a configuration close to the experimental one by HBG, including a local forcing, the confinement effect by the walls, and solid body rotation. We briefly recall previous works on diffusive turbulence obtained by an oscillating grid, and we present statistical results in the rotating case, analysed with the help of two- and three-dimensional visualizations. More specifically we shall try to observe the structural transition that is expected between a region close to the grid, where the

flow is not influenced by rotation, and a region far away where the Coriolis force is dominant in the dynamics of the flow, leading to the appearance of vortical structures almost aligned with the rotation vector.

2. Effects of the Coriolis force on fluid motion

2.1. *Equations in a rotating frame*

We recall here the motion equations of a Newtonian fluid in a rotating frame. An extensive presentation is given by Greenspan (1968), to which the reader is referred for details. The rotation vector is $\boldsymbol{\Omega}$. The quantities $\boldsymbol{u}$, $\boldsymbol{r}$, t, p, ρ, v and $\boldsymbol{f}$ are respectively the fluid velocity in the rotating frame, position vector, time, pressure, density, kinematic viscosity and volume forces per unit mass. The mass and momentum conservation equations, i.e. the Navier–Stokes equations, are therefore

$$\nabla \cdot \boldsymbol{u} = 0, \tag{2.1}$$

$$\frac{\partial \boldsymbol{u}}{\partial t} + \boldsymbol{u} \cdot \nabla \boldsymbol{u} = -\nabla \Pi - 2\boldsymbol{\Omega} \times \boldsymbol{u} + v\nabla^2 \boldsymbol{u}. \tag{2.2}$$

We have supposed here that body forces derive from a scalar potential such that $\boldsymbol{f} = -\nabla\phi$, as is the case for the centrifugal force, which can be expressed as $\nabla(\boldsymbol{\Omega} \times \boldsymbol{r})^2/2$. The pressure Π is a modified pressure given by

$$\Pi = \frac{p}{\rho} + \phi - \tfrac{1}{2}(\boldsymbol{\Omega} \times \boldsymbol{r})^2.$$

Non-dimensionalizing the systems brings two non-dimensional numbers, based on a reference length L and velocity U. Equation (2.2) becomes, in non-dimensional form

$$\frac{\partial \boldsymbol{u}}{\partial t} + \boldsymbol{u} \cdot \nabla \boldsymbol{u} = -\nabla \Pi - Ro^{-1}\boldsymbol{x} \times \boldsymbol{u} + Re^{-1}\nabla^2 \boldsymbol{u}, \tag{2.3}$$

assuming, without loss of generality, that $\boldsymbol{\Omega}$ is carried by the unit vector $\boldsymbol{x}$. The Reynolds number $Re = UL/v$ is the ratio between inertial and viscous effects, and the Rossby number $Ro = U/(2\Omega L)$ gives the relative importance of the inertial effects with respect to the rotation ones. One can define an Ekman number $Ek = v/2\Omega L^2$ as the ratio between the Rossby and the Reynolds numbers.

In equation (2.2), the term $-2\boldsymbol{\Omega} \times \boldsymbol{u}$ acts in the plane orthogonal to the rotation axis, and represents the acceleration due to the Coriolis force. Two remarks can be made about this force. First it does not produce work, since the force is always perpendicular to velocity, so that it cannot bring energy to the fluid. Second, in the case of two-dimensional flows in a plane orthogonal to $\boldsymbol{\Omega}$, the Coriolis acceleration can be included in the modified pressure term, so that it does not appear any more in the system of equations, which become identical to the equations in the non-rotating case. This is a reason for the necessity, in linear stability analyses of two-dimensional rotating flows, for the perturbation to be three-dimensional in order to get any modification of the base flow by the perturbation.

2.2. *Numerical and experimental approaches*

A pioneering study on rotation was done by Taylor (1921), for the slow motion of a cylinder or sphere in a rotating fluid. The solid body motion of the fluid in the wake of the obstacle is nowadays well known as Taylor columns. Later works on the effect of rotation on turbulence include Ibbetson & Tritton (1975), Wigeland & Nagib (1978), Hopfinger *et al.* (1982), Jacquin (1987). The differences between these various

experiments lie mainly in the origin of the turbulence. Wigeland & Nagib, as well as Jacquin, use grid turbulence. Ibbetson & Tritton create the initial flow by a towed grid in a tank filled with fluid at rest. Hopfinger *et al.* use an oscillating grid in a rotating tank. A detailed comparison of these experiments is given in Jacquin (1987), and in Jacquin *et al.* (1990), with emphasis on the degree of homogeneity of the turbulence obtained, and the relative importance of inertial waves. Apart from over-dissipation due to the reflection of inertial waves observed by Ibbetson & Tritton, these studies all agree in that rotation creates anisotropy and reduces the energy transfers. In such an anisotropic flow, evolving towards two-dimensionality, one may look for evidence of an inverse cascade, as done by Hossain (1996), who considered as well the case of magnetofluid turbulence that exhibits comparable structural properties. In rotating flows, a very strong two-dimensional manifold, i.e. when a large part of the energy is concentrated towards horizontal wavevectors, may contain a discernible inverse transfer of energy, from small to large scales. A spectral wave-band forcing has also been identified as a good means of achieving this inverse cascade. However, when the two-dimensional manifold is immersed in a still non-negligible three-dimensional field of scrambled inertial waves, as in our simulations, one is not able to observe this inverse cascading process, and in the following we will not dwell more upon this point. Though well-suited for reproducing a close-to-isotropic diffusive layer, our forcing (see § 6.4) introduces unphased periodic perturbations that drown some of the structural coherence in the whole flow.

Different from fully developed turbulence experiments, linear effects of rotation have been observed in the form of inertial waves by McEwan (1970) and Heikes & Maxworthy (1982), who generated them by introducing a local forcing in a rotating tank. Although their experimental apparatus is different, they both confirm the propagation of energy by waves, in directions prescribed by the rotation rate. McEwan's visualizations, using an isolated steering device, exhibit cross-shaped patterns. Note also that the strong analogy between inertial and internal gravity waves can be seen by comparing his experiment to that of Mowbray & Rarity (1967). The latter authors introduce a local forcing in a tank filled with density stably stratified fluid, and observe the same kind of patterns. The internal gravity waves, in that case, are produced by the restoring buoyancy force undergone by fluid particles of given density displaced from their original stable height.

In general, real turbulent flows or industrial ones are not only subjected to the Coriolis force, but also to many external effects such as those induced by a sheared mean flow, and the presence of solid boundaries. Couette and Poiseuille flows have been the focus of many theoretical studies. The combination of shear and rotation has been studied by Tillmark & Alfredsson (1996) for Couette flow. They show evidence of the structuring effect of rotation by the emergence of organized structures in the stable case. In the same way, for rotating channel flow, Johnston, Halleen & Lezius (1972), confirm the existence of a stabilized region – eventually re-laminarized on the cyclonic side – and of a destabilized one. Organized vortices in a rotating frame can combine the effects of shear, rotation and curvature. Isolated vortices were studied by Kloosterziel (1990) and Carnevale *et al.* (1997). The review paper by Hopfinger & van Heijst (1993) establishes links with the stability of actual vortices, either atmospheric or oceanic.

2.3. *Linear stability of rotating flows*

Within a given range, solid body rotation can modify the stability properties of coherent structures existing in turbulent flows, although it cannot explain the generation of

such organised motion. An example from everyday life is atmospheric vortices that, at average latitudes, seem to be stable because of their longlife, due to the stabilizing effect of the Earth's rotation. Kloosterziel (1990) observes that experimentally it is easy to create a cyclonic vortex by local forcing whereas any attempt at creating an anti-cyclone leads to mixed inertial waves and turbulence. He also observes that cyclonic vortices can move, be distorted or pair up, while remaining globally stable. Linear stability analyses have provided criteria for the stability of some classes of flows, as in Pedley (1969) in the pure shear case, Kloosterziel (1990) for circular vortices, and Craik (1989) for the elliptic vortex. In the more general case of quadratic base flows, where the velocity gradient is uniform and has either hyperbolic, straight or elliptic streamlines, stability criteria are obtained by Cambon *et al.* (1994) followed by a numerical study of Taylor–Green vortices in a rotating frame. All these works recover the classical stability criterion that uses pressureless modes and compares the relative vorticity W to that of the rotating frame 2Ω. In all cases, the base flow is two-dimensional and the perturbation has to be three-dimensional in order for the rotation effect to act at all. For example, in a one-directional sheared flow $U = U(y)$ in a Cartesian frame rotating at Ω, instability appears locally if the criterion by Pedley (1969) holds, that is

$$2\Omega(2\Omega + W) < 0,$$

with $W = -\mathrm{d}U/\mathrm{d}y$. The same criterion was found from a semi-empirical analysis by Bradshaw (1969) and can describe the stabilization or destabilization of rotating shear flows, even strongly turbulent ones, in agreement with experiments and simulations by Johnston *et al.* (1972) or Kristoffersen & Andersson (1993). Finally Leblanc (1997) and Leblanc & Cambon (1997) extend this criterion to a wider class of non-viscous two-dimensional flows with complex topologies. Generally speaking, these stability studies all lead to the conclusion that strong anti-cyclones are unstable, when W is now taken as the vorticity in the core of the vortex. Our results on forced rotating turbulence in § 6.6.4 are consistent with this conclusion.

2.4. *Nonlinear aspects of the structuring of turbulent flows by rotation*

The evolution of complex turbulent and/or unsteady flows is also modified in a nonlinear manner by background rotation. In the case of homogeneous turbulence, it is now recognized that rotation can act on the structure of the flow in a nonlinear way only, by modification of redistribution terms for energy.

Consider the case of initially isotropic freely decaying homogeneous turbulence. Without rotation, the evolution of such flows has been extensively studied. The integral length scale, unique in isotropic turbulence, grows with time, approximately as $t^{0.35}$, while the kinetic energy decays as $t^{-1.3}$ (the values of these exponents can vary depending on the small-wavenumber behaviour of the initial spectrum). When the Coriolis force is present, it has been shown by Jacquin (1987); Jacquin *et al.* (1990) and Cambon *et al.* (1997), that two Rossby numbers are necessary for describing the effect of rotation on turbulence. The first effect of rotation starts when a macroscopic Rossby number Ro^L, based on the integral length scale, is close to unity. A departure from isotropy is then indicated by a growth of integral length scales with vertical separation, and a decrease of those with horizontal separation. This is the sign that a transition process is triggered, during which rotation acts upon the nonlinear transfer terms. The end of this period is characterized by a unit microscopic Rossby number Ro^ω, the ratio of the local vorticity to the background one. The flow is then essentially driven by linear effects, that combine the viscous decay and the inertial waves (see

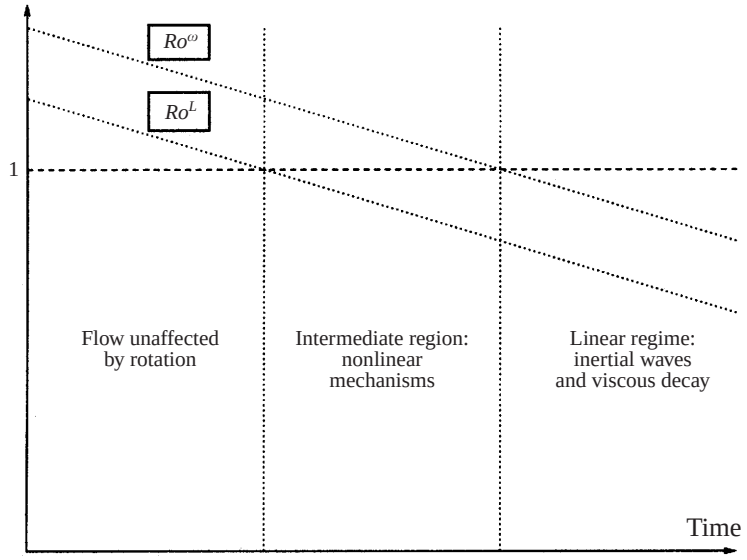

FIGURE 2. Different regimes encountered by freely decaying initially isotropic homogeneous turbulence subjected to solid body rotation.

figure 2). However, although rotation creates anisotropy, as shown by integral length scales, no clear-cut structuring appears, e.g. in the shape of strong and long-lived coherent structures. On the other hand, Dang & Roy (1985) show that if one chooses the initial field as the superposition of two-dimensional vortices (large scales) aligned with the rotation axis, and three-dimensional perturbations (small scales), a strong rotation kills the perturbations. Only the two-dimensional vortices, initially immersed in the turbulent field, remain, since the small scales are dissipated by viscous effects, and are no longer fed energy from the large scales, for the cascade of energy is damped by rotation.

3. Numerical method and definitions

In the following we describe the method of direct numerical simulations we have used, focusing on the original decomposition of the fields into a set of functions that verify implicitly the solenoidal property, as well as the conditions at the walls. Our method is a pseudo-spectral one. Let us also point out that our simulations have a Reynolds number which should ideally be much larger, but is still unattainable by the current computer capacities. In the case of isotropic homogeneous turbulence, solving both the largest energetic (integral length L) and smallest dissipative scales (Kolmogorov length η) in the flow imposes a constraint on the resolution depending on the Reynolds number: $Re \propto (L/\eta)^{4/3}$. The smallest numerical grid size Δx should therefore be of the order of η, and if the box has size $N\Delta x$, N being the number of discretized points along one direction of space, we get the relation $(L/\eta) \approx N \propto Re^{3/4}$ which gives the upper limit for Re. However we have not used large-eddy simulations, for the introduction of a given subgrid-scale model, still to be greatly improved in the case of rotating flow, leads to uncontrolled side effects, which sometimes make the conclusions rather far away from the actual physics of turbulent flows. In the forced case, we have checked that the energy introduced by the forcing is carried by a wavenumber that lies within the resolved range, i.e. corresponding to the smallest

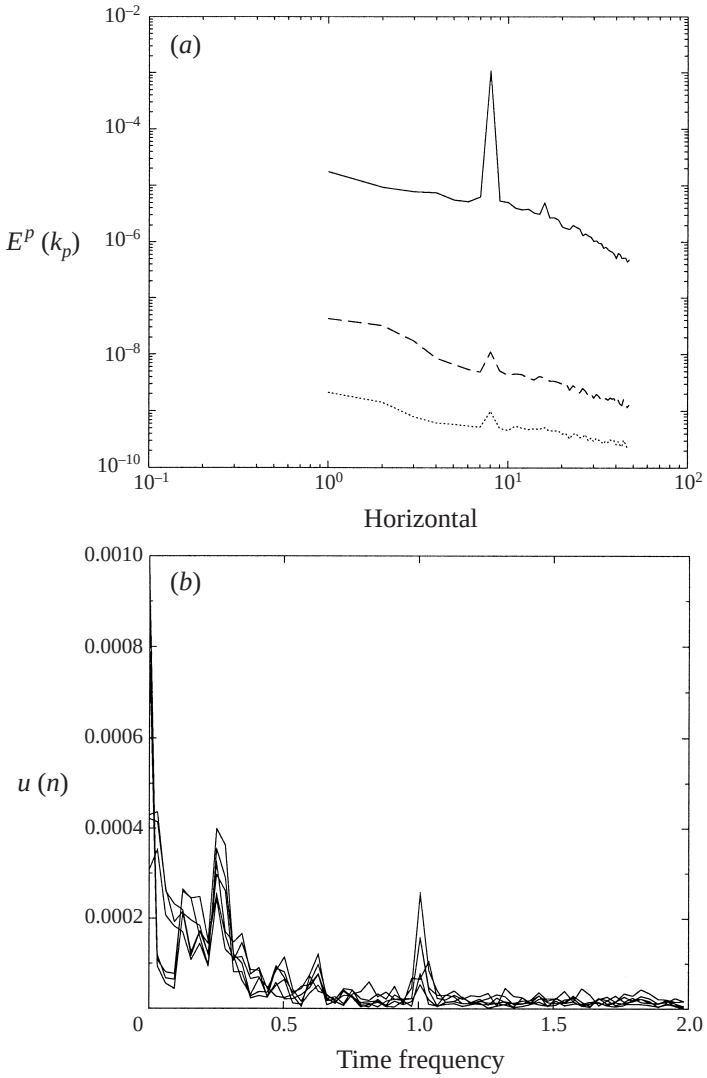

FIGURE 3. (*a*) One-dimensional spectra, averaged in the two horizontal directions $p = 2, 3$, at different locations from the forcing plane. · · · · , $x' = 6.7$; — — , $x' = 3.4$; —— , $x' = 0$ (x' is defined as the distance to the grid). (*b*) Time series spectra recorded for the horizontal components at different locations in the flow domain. The time frequency of the grid is found at $n = 1$.

resolved scales in the flow, at least in the region of the forcing plane. The peak of the forcing appears clearly on figure 3(*a*), corresponding to the characteristic space frequency of the grid. Figure 3(*b*) also shows time frequency spectra of the horizontal component of the velocity at different locations away from the grid. On these, the oscillating frequency of the grid, set to 1, can also be observed.

3.1. *Moser, Moin & Leonard's numerical method for a three-dimensional channel*

3.1.1. *Equations*

We consider the unsteady Navier–Stokes equations for a channel flow between two parallel plane walls with infinite extent in the y (or x_2) and z (or x_3) directions. Hence, the flow is assumed to be periodic in these two directions. The inhomogeneous

direction, that is normal to the walls, is x (or x_1). (Please note that this choice is different from the usual one, especially for presenting experimental results of channel flows.) The computational domain has a size $2L_1 \times L_2 \times L_3$. Finally, by a simple geometrical transformation, non-dimensional lengths are used in the code for mapping the channel to a more convenient $[-1;1] \times [0;2\pi] \times [0;2\pi]$ size, in accordance with our use of Chebyshev and Fourier polynomials. The system of equations which is numerically solved is constituted by the mass and momentum conservation equations for an incompressible fluid which are in dimensional form

$$\left.\begin{aligned} \frac{\partial \boldsymbol{u}}{\partial t} + (\boldsymbol{\omega} + 2\boldsymbol{\Omega}) \times \boldsymbol{u} = -\nabla \Pi + \nu \nabla^2 \boldsymbol{u}, \\ \nabla \cdot \boldsymbol{u} = 0, \end{aligned}\right\} \tag{3.1}$$

with the constraint that $\boldsymbol{u}$ be zero at the walls. The vorticity $\boldsymbol{\omega} = \nabla \times \boldsymbol{u}$ is used for writing the convective terms in the first equation of (3.1), so that the modified pressure appears here as $\Pi = p/\rho + |\boldsymbol{u}|^2/2 - \Omega^2 r^2/2$, with $r = |\boldsymbol{r}|$.

3.1.2. *Numerical method*

The method presented here was first proposed by Moser, Moin & Leonard (1983) and is also presented by Canuto *et al.* (1988); an extensive description of the numerical method is also given in Pasquarelli, Quateroni & Sacchi-Landriani (1987). The goal is to project the velocity field onto a base of spatial functions that each verify the boundary non-slip conditions at the walls, and the solenoidal property. By use of this space of functions, the gradient of the fluctuating pressure disappears from the system of equations, while still retaining the ability of imposing a mean pressure gradient in the horizontal homogeneous directions. In all our simulations, we shall however assume that this gradient is zero, therefore avoiding the appearance of a driving force that would create a non-zero mean velocity.

The velocity field is decomposed into a combination of Fourier modes in the two periodic directions, and into linear combinations of Chebyshev polynomials in the wall-normal direction, such that the non-slip condition is exactly verified by these modes at the walls. The weak formulation of our system of equations is written by choosing test functions that are identical to the decomposition ones, making our method of Galerkin type. As an additional constraint, we impose that the velocity field, and the test functions, verify implicitly the divergenceless property. The initial hypotheses are then (with $\mathrm{i}^2 = -1$), for the velocity field

$$\boldsymbol{u}(x,y,z,t) = \sum_{i=0}^{n_x} \sum_{k_y=-n_y/2}^{n_y/2-1} \sum_{k_z=-n_z/2}^{n_z/2-1} \alpha_{ik_yk_z}(t) \tilde{\boldsymbol{u}}_i(x,k_y,k_z) \exp\left[\mathrm{i}(k_y y + k_z z)\right], \tag{3.2}$$

$$\nabla \cdot \left[\tilde{\boldsymbol{u}}_i(x,k_y,k_z) \exp \mathrm{i}(k_y y + k_z z)\right] = 0, \tag{3.3}$$

$$\tilde{\boldsymbol{u}}_i(\pm 1, k_y, k_z) = 0; \tag{3.4}$$

and for the test functions

$$\boldsymbol{\phi}(x,y,z) = \sum_{i=0}^{n_x} \sum_{k_y=-n_y/2}^{n_y/2-1} \sum_{k_z=-n_z/2}^{n_z/2-1} \tilde{\boldsymbol{\phi}}_i(x,k_y,k_z) \exp\left[\mathrm{i}(k_y y + k_z z)\right], \tag{3.5}$$

$$\nabla \cdot [\tilde{\boldsymbol{\phi}}_i(x,k_y,k_z) \exp \mathrm{i}(k_y y + k_z z)] = 0, \tag{3.6}$$

$$\tilde{\boldsymbol{\phi}}_i(\pm 1, k_y, k_z) = 0. \tag{3.7}$$

The scalar product between functions is defined as

$$\langle \boldsymbol{u}, \boldsymbol{\phi} \rangle = \int_{\Omega} \boldsymbol{u} \cdot \boldsymbol{\phi}\, \omega \, \mathrm{d}\Omega, \tag{3.8}$$

where $\omega(x) = 1/(1-x^2)^{1/2}$ is the weighting function that ensures the orthogonal property of Chebyshev polynomials in (3.8). By plugging (3.2) in the Navier–Stokes system (3.1), and upon taking the scalar product with the test functions (3.5), one gets the following equations:

$$\left\langle \frac{\partial \boldsymbol{u}}{\partial t}, \boldsymbol{\phi} \right\rangle = \nu \left\langle \nabla^2 \boldsymbol{u}, \boldsymbol{\phi} \right\rangle - \left\langle (\nabla \times \boldsymbol{u}) \times \boldsymbol{u}, \boldsymbol{\phi} \right\rangle. \tag{3.9}$$

The pressure term $\langle \nabla \Pi, \boldsymbol{\phi} \rangle$ cancels out, since it amounts to $-\langle \nabla \phi, \Pi \rangle$, where $\nabla \phi = 0$ by construction. For each pair of wavenumber components (k_y, k_z), the following linear matrix system is to be solved:

$$\boldsymbol{A} \frac{\mathrm{d}\boldsymbol{\alpha}}{\mathrm{d}t} = \nu \boldsymbol{B} \boldsymbol{\alpha} + \boldsymbol{F}, \tag{3.10}$$

where $\boldsymbol{\alpha} = (\alpha_0, \alpha_1, \ldots, \alpha_{n_x})$ is the vector of unknown spectral coefficients at these given (k_y, k_z) – we have dropped the last two indices of α – that appeared in (3.2) – and $\boldsymbol{A}$ and $\boldsymbol{B}$ are matrices of dimensions $(n_x + 1) \times (n_x + 1)$. Their components write are

$$A_{ij} = \langle \tilde{\boldsymbol{u}}_i, \tilde{\boldsymbol{\phi}}_j \rangle$$

and

$$B_{ij} = \left\langle \frac{\mathrm{d}^2 \tilde{\boldsymbol{u}}_i}{\mathrm{d}x^2} - (k_y^2 + k_z^2) \tilde{\boldsymbol{u}}_i, \tilde{\boldsymbol{\phi}}_j \right\rangle,$$

and $\boldsymbol{F}$ accounts for the nonlinear terms that are associated with a forcing.

The vector functions $\tilde{\boldsymbol{u}}$ and $\tilde{\boldsymbol{\phi}}$ are in turn decomposed on the basis of orthogonal divergenceless vectors. Indeed, due to the incompressibility of the fluid, two vectors are enough for decomposing the velocity field. (In a complete three-dimensional Fourier description, the spectral component of the solenoidal velocity lies in the plane orthogonal to the corresponding wavevector.) The choice of this basis is not unique, but one has to choose the one that leads to a well-conditioned linear system, i.e. to sparse matrices. Let $(\boldsymbol{e}_i^+(x), \boldsymbol{e}_i^-(x))$ and $(\boldsymbol{f}_i^+(x), \boldsymbol{f}_i^-(x))$ be the divergenceless bases onto which are decomposed $\tilde{\boldsymbol{u}}_i$ and $\tilde{\boldsymbol{\phi}}_i$. This yields:

$$\begin{aligned} \tilde{\boldsymbol{u}}_i(x) &= u_i^+ \boldsymbol{e}_i^+(x) + u_i^- \boldsymbol{e}_i^-(x), \\ \tilde{\boldsymbol{\phi}}_i(x) &= \boldsymbol{f}_i^+(x) + \boldsymbol{f}_i^-(x). \end{aligned}$$

These two different bases are orthogonal, so that $\langle \boldsymbol{e}^+, \boldsymbol{f}^- \rangle = 0$ and $\langle \boldsymbol{e}^-, \boldsymbol{f}^+ \rangle = 0$. Using the notation $k_h = \sqrt{k_y^2 + k_z^2}$ for the horizontal Fourier component, they can also be written (prime is used instead of $\partial/\partial x$)

$$\boldsymbol{e}_j^+(x) = \begin{Bmatrix} k_h g_j(x) \\ \mathrm{i} k_y g_j'(x)/k_h \\ \mathrm{i} k_z g_j'(x)/k_h \end{Bmatrix}, \qquad \boldsymbol{e}_j^-(x) = \begin{Bmatrix} 0 \\ -k_z h_j(x)/k_h \\ k_y h_j(x)/k_h \end{Bmatrix},$$

$$\boldsymbol{f}_l^+(x) = \left\{ \begin{array}{c} k_h Q_l(x) \\ \dfrac{\mathrm{i}}{\omega} k_y \left(Q_l(x)\omega(x)\right)' / k_h \\ \dfrac{\mathrm{i}}{\omega} k_z \left(Q_l(x)\omega(x)\right)' / k_h \end{array} \right\}, \qquad \boldsymbol{f}_l^-(x) = \left\{ \begin{array}{c} 0 \\ -k_z P_l(x)/k_h \\ k_y P_l(x)/k_h \end{array} \right\}.$$

Given each pair of wavenumber components (k_y, k_z), this leads to a pair of system equations that include the two independent components of the incompressible velocity field, namely α_i^+ and α_i^- (hence we have to deal with $2 \times n_y \times n_z$ systems of equations). Depending upon (k_y, k_z), the following two systems are thus written:

$$\boldsymbol{A}^+ \frac{\mathrm{d}\boldsymbol{\alpha}^+}{\mathrm{d}t} = \nu \boldsymbol{B}^+ \boldsymbol{\alpha}^+ + \boldsymbol{F}^+,$$

$$\boldsymbol{A}^- \frac{\mathrm{d}\boldsymbol{\alpha}^-}{\mathrm{d}t} = \nu \boldsymbol{B}^- \boldsymbol{\alpha}^- + \boldsymbol{F}^-.$$

The basis functions g_j and h_j are here chosen to be the Chebyshev polynomial $T_j(x)$ weighted by a simple function of the variable $(1 - x^2)$, which verifies the boundary conditions in the x-direction for the velocity. We then get the following expressions:

$$\left. \begin{array}{r} g_j(x) = (1-x^2)^2 T_j(x), \\ h_j(x) = (1-x^2) T_j(x), \\ g_j(x = \pm 1) = 0, \quad g_j'(x = \pm 1) = 0, \quad h_j(x = \pm 1) = 0. \end{array} \right\} \tag{3.11}$$

Finally, choosing carefully the test functions $Q_l(x)$ and $P_l(x)$ allows one to obtain sparse matrices $\boldsymbol{A}^+$, $\boldsymbol{A}^-$, $\boldsymbol{B}^+$ and $\boldsymbol{B}^-$, though non-symmetric (they have respectively 7 and 4 non-zero diagonals). The choice is combinations of Chebyshev polynomials, as proposed by Moser *et al.*:

$$Q_l(x) = \frac{1}{4} \left[\frac{T_{l+4}(x)}{(l+2)(l+3)} - \frac{2T_{l+2}(x)}{(l+1)(l+3)} + \frac{T_l(x)}{(l+2)(l+1)} \right],$$

$$P_l(x) = \frac{T_l(x) - T_{l+2}(x)}{2(l+1)}.$$

The resolution of the two previous linear systems ultimately leads to the spectral coefficients of the velocity field, which can be transformed back to physical space.

3.1.3. *Time scheme*

The time variable is discretized using a constant time step Δt. Assuming the velocity field at time t^n is known, the time-discretized momentum equations are used to get the field at instant t^{n+1}. Linear and nonlinear terms in the equations are treated differently (see Kim & Moin 1985). The unsteady term $\partial \boldsymbol{u}/\partial t$ is computed as $(\boldsymbol{u}^{n+1} - \boldsymbol{u}^n)/\Delta t$, while the nonlinear term $\mathrm{NLI}(\boldsymbol{u}^{n+1})$ is evaluated by the explicit order-two Adams–Bashforth one $(3\,\mathrm{NLI}(\boldsymbol{u}^n) - \mathrm{NLI}(\boldsymbol{u}^{n-1}))/2$. In so doing, it is therefore necessary to store the nonlinear terms at instant t^{n-1}. The linear operator $\boldsymbol{L} = \nu \nabla^2$ is discretized by a second-order Crank–Nicholson numerical scheme, with the unknown implicit part $\boldsymbol{L}(\boldsymbol{u}^{n+1})/2$ moved to the left-hand side of the equations. Finally, one gets the discretized equation

$$\left(\boldsymbol{I} - \tfrac{1}{2}\Delta t \boldsymbol{L}\right) \boldsymbol{u}^{n+1} = \left(\boldsymbol{I} + \tfrac{1}{2}\Delta t \boldsymbol{L}\right) \boldsymbol{u}^n - \tfrac{1}{2}\Delta t \left[3\,\mathrm{NLI}(\boldsymbol{u}^n) - \mathrm{NLI}(\boldsymbol{u}^{n-1})\right], \tag{3.12}$$

where $\boldsymbol{I}$ is the unit operator.

3.2. *Computation of statistical quantities*

We shall study the turbulent flows obtained in our simulations by examining miscellaneous one- and two-point statistical quantities whose definitions are given hereafter. Due to the cost of the simulations, it is not possible to obtain many realizations of the same turbulent flow with identical macroscopic parameters, over which ensemble averaging should ideally be performed. We rather use the spatial homogeneity of the flow in horizontal planes, and time averaging in the statistically steady runs, to obtain statistics that seem accurate enough. Therefore, spatial averaging is performed along the homogeneous planes (x_2, x_3), parallel to the walls, and is denoted $\langle\cdot\rangle$. Using Reynolds' decomposition, any variable ϕ is split in its mean $\langle\phi\rangle$ and its fluctuating part ϕ', such that $\phi = \langle\phi\rangle + \phi'$. Root mean square values are obtained as $\phi_{\text{r.m.s.}} = \sqrt{\langle(\phi - \langle\phi\rangle)^2\rangle}$.

Our analysis of statistical quantities is based on the knowledge we already have of the evolution of homogeneous rotating turbulence. Accordingly, we shall first investigate dynamical energetic quantities. The turbulent kinetic energy is $q^2/2 = \langle u_i u_i\rangle/2$ and is dissipated at rate $\varepsilon = 2\nu\langle S_{ij}S_{ij}\rangle$ where S_{ij} is the strain rate tensor $S_{ij} = \left(u_{i,j} + u_{j,i}\right)/2$. We also compute the skewness of velocity derivatives as (see Batchelor 1953)

$$S_{u_i} = \langle u_{i,i}^3\rangle/\langle u_{i,i}^2\rangle^{3/2} \quad \text{(no summation on } i\text{)}. \tag{3.13}$$

This coefficient is commonly used for characterizing the energy transfers arising in homogeneous turbulent flow through triple correlations of the velocity. It is usually of the order of $S \approx -0.3$ in isotropic homogeneous fully developped turbulence, and we shall compare this value to the ones we obtain in the inhomogeneous configuration. More specifically, we will distinguish between skewness coefficients based on the vertical component of the velocity, S_v and those based on the horizontal one S_h.

Then, one-dimensional spectra are obtained by Fourier transforms of the correlation functions $\mathrm{R}_{ij}(x_p) = \langle u_i(x)u_j(x + x_p)\rangle$ of the components u_i and u_j of the velocity in direction x_p. The one-dimensional spectrum in that direction is therefore

$$E_{ij}^p(k_p) = \frac{1}{2\pi}\int_{-\infty}^{\infty} \mathrm{R}_{ij}(x_p)\mathrm{e}^{-\mathrm{i}k_p x_p}\mathrm{d}x_p. \tag{3.14}$$

In the following, we will examine E_{11}^p, E_{22}^p and E_{33}^p with $p = 2, 3$ (homogeneous directions), and we shall discuss the kinetic energy spectrum obtained as the trace of the above spectral tensors, $E^p = E_{ii}^p/2$. The three-dimensional spectrum, computed by integration over spherical shells in spectral space, in the case of homogeneous computations will be denoted $E(k)$.

Following Jacquin *et al.* (1990) and Cambon *et al.* (1997), who have studied the case of rotation homogeneous turbulence, we will qualify the regime of our rotating turbulent flow by using two different Rossby numbers, one a macro-Rossby number, based on the integral length scale, and the other one based on the Taylor microscale: respectively $Ro^L = u/(2\Omega L)$ and $Ro^\omega = \omega/(2\Omega)$, where u and ω are r.m.s. values for velocity and vorticity.

In order to give a precise view of the large-scale anisotropy and structuring of the flow, directional integral length scales are calculated:

$$L_{ii,j}(\boldsymbol{x}) = \frac{1}{2}\int_{-\infty}^{\infty} \frac{\langle u_i(\boldsymbol{x})u_i(\boldsymbol{x} + r\boldsymbol{n}_j)\rangle}{\langle u_i^2(\boldsymbol{x})\rangle}\mathrm{d}r \quad \text{(no summation on } i\text{)}, \tag{3.15}$$

where $\boldsymbol{n}_j$ is the unit vector in direction x_j. The total number of these is nine, but we will

limit our discussion to the two most interesting ones, associated with the correlation of the horizontal velocity component with vertical and horizontal separation distances. They are computed as $L_{h,h} = \frac{1}{2}(L_{22,2} + L_{33,3})$ and $L_{h,v} = \frac{1}{2}(L_{22,1} + L_{33,1})$.

Finally we consider the deviatoric part of the Reynolds stress tensor, defined as $b_{ij} = \langle u_i u_j \rangle / q^2 - \delta_{ij}/3$, which is zero in isotropic homogeneous turbulence. The component b_{11} will be computed as $b_{11} = \langle u_1^2 \rangle / q^2 - \frac{1}{3}$. In our context, b_{11} is the most important component to look at, since it shows the relative importance of the vertical motion compared to the horizontal one, and its value reflects wall effects, Ekman pumping, and the fact that there exists a vertical component of velocity in the vertically aligned vortices.

4. Inertial waves

4.1. *Predictions of the non-viscous linear theory*

Considering a non-viscous fluid, one can derive the dispersion law for inertial waves from the linearized system of Navier–Stokes equations (2.2) in a rotating frame:

$$\frac{\partial \boldsymbol{u}}{\partial t} + 2\boldsymbol{\Omega} \times \boldsymbol{u} = -\nabla \pi, \tag{4.1}$$

$$\nabla \cdot \boldsymbol{u} = 0, \tag{4.2}$$

where $\pi = p/\rho - (\boldsymbol{\Omega} \times \boldsymbol{r})^2 /2$. Real valued solutions are sought in the shape of plane waves by writing

$$\boldsymbol{u}(\boldsymbol{x}, t) = \mathrm{Re}\left\{ \boldsymbol{U}(\boldsymbol{k}) \exp\left[\mathrm{i}(\boldsymbol{k} \cdot \boldsymbol{x} + \sigma t)\right] \right\},$$

$$\pi(\boldsymbol{x}, t) = \mathrm{Re}\left\{ \Pi(\boldsymbol{k}) \exp\left[\mathrm{i}(\boldsymbol{k} \cdot \boldsymbol{x} + \sigma t)\right] \right\}.$$

Upon substitution of these in (4.1), and after a bit of algebra (see Greenspan 1968), one gets the desired dispersion relation

$$\sigma = \pm 2\Omega \cos\theta. \tag{4.3}$$

In the above equation, θ is the angle between the rotation vector and the wavevector (see figure 5). This dispersion relation for inertial waves shows the anisotropic character of these waves, whose propagation is only related to the orientation of the wavevector, with no explicit limitation on their wavelength, since, *a priori*, any wavenumber $k = |\boldsymbol{k}|$ is possible. Only the time frequency σ is bounded and less than 2Ω. This comes from the fact that the wave propagation is ruled by the Poisson equation

$$\frac{\partial^2}{\partial t^2} \nabla^2 \Phi = 4\Omega^2 \frac{\partial^2 \Phi}{\partial x_1^2},$$

where Φ can be either the pressure or the velocity component parallel to the rotation vector. This equation is hyperbolic only when $4\Omega^2 > \sigma^2$, and, in that case, admits wave solutions. When $4\Omega^2 < \sigma^2$, it is of elliptic type, and no physical waves can propagate in the fluid.

Using (4.3) one may derive the phase and group velocities as $\boldsymbol{c}_\phi = (2\boldsymbol{\Omega} \cdot \boldsymbol{k})\boldsymbol{k}/k^3$ and $\boldsymbol{c}_g = \nabla_k \sigma = \boldsymbol{k} \times (2\boldsymbol{\Omega} \times \boldsymbol{k})/k^3$. Iso-phase lines, or crest lines, are moving with velocity $\boldsymbol{c}_\phi$, while the energy propagates at $\boldsymbol{c}_g$, i.e. parallel to the lines of constant phase, illustrating the fact that inertial waves are transverse ones. One distinguishes more specifically two different regimes. In the case of $\theta = \pi/2$, the ratio $\sigma/(2\Omega) = 0$, whence the corresponding wave is stationary. In that case, the wavevector is horizontal and

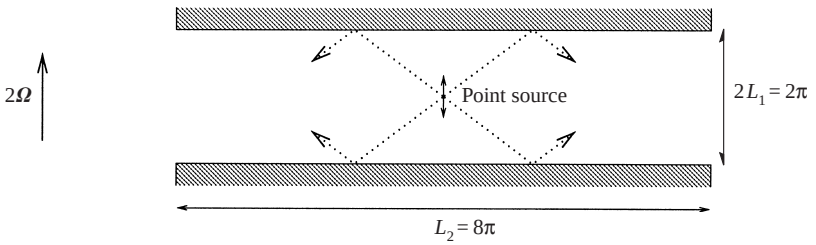

FIGURE 4. Sketch of the numerical experiment geometry used for generating the inertial waves.

the iso-phase lines are vertical and do not move, since their velocity is zero. On the other hand, the energy propagates vertically, an indicator of possible vertical motion. The pressure gradient also compensates exactly the Coriolis force, in a geostrophic equilibrium. When $\theta = 0$, iso-phase lines are horizontal and no energy propagation is allowed as the group velocity cancels out. The unsteady term compensates exactly the Coriolis force in that case.

Solid boundaries can interact with the propagation of inertial waves by allowing a linear transfer of energy between wavevectors, by reflection (see Phillips 1963), provided the local boundary tangent orientation is neither parallel nor orthogonal to the rotation axis of the fluid. In that case, the reflected wave has a different wavenumber than the incident one, producing net transfer of energy within the inertial wave spectrum.

Analogous to the inertial waves in rotating flows, internal gravity waves appear in stably stratified flows. Both are very similar in effect, and the reader is referred to the paper by Veronis (1970) for an extensive discussion of the analogy. For the stably stratified case, a mean density (or temperature) gradient leads to the appearance of a characteristic frequency N of the internal gravity waves, and can be associated with a rotation rate. The mathematical nature of these waves is very close to that of inertial ones, with the difference that their dispersion relation behaves as $\sigma = \pm N \sin\theta$, leading to reverse tendencies in particular propagation directions with respect to inertial waves.

4.2. *Numerical simulations of inertial waves*

4.2.1. *Geometry and parameters*

On figure 4 we show the geometry we have used for the simulation of the inertial waves. The computational domain in the horizontal direction is chosen such that reflection at the walls can occur before the wave reaches the periodic boundary, leading to an aspect ratio of 4 for the channel. The initiation of the waves, i.e. the localized forcing, is performed by introducing a sine acceleration at one point, with a given time frequency ($n = 1$ here). Each simulation's duration corresponds to at least twenty forcing periods, while ensuring again that waves do not reach the periodic boundaries, a situation which would lead to unphysical results, since periodicity would artificially modify the kinematics of the waves. The molecular viscosity has been set to an almost zero value to avoid too strong a damping of the energy propagation, and the resolution is shown to be possibly relatively low (here $32 \times 64 \times 64$ points) without impairing the accuracy of the results. The parameters of the different simulations are shown in table 1. Visualizations are done at the end of the simulations, showing the lines of constant phase, or wave crests. The angle between these and the horizontal direction is therefore θ (as in figure 5).

$2\Omega/n$	1.10, 1.33, 2
ν	10^{-7}
Oscillation amplitude A	0.1
Velocity scale	0.1
Reynolds (forcing) nA^2/ν	$\approx 10^5$

TABLE 1. Parameters for the linear simulations for the inertial waves regime.

$2\Omega/n$	θ theory (deg.)	θ measurement (deg.)
1.10	25	26
1.33	41	42
2.00	60	62

TABLE 2. Measured angles in the visualisations for the different wave propagation directions given by the different rotation rates.

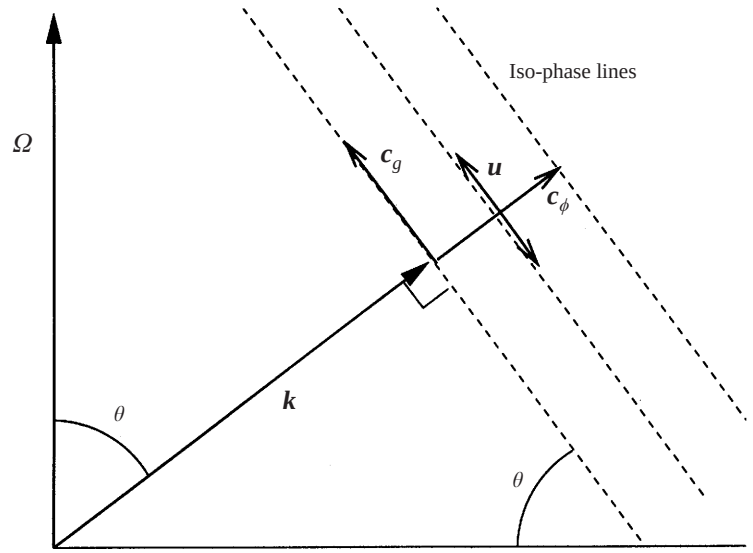

FIGURE 5. Dynamics of inertial waves. Dashes indicate lines of constant phase, aligned with the group velocity of the waves and the velocity vector.

4.2.2. *Results*

In the following, angles are manually measured, to very good accuracy, with an error less than $\pm 2^\circ$. Figure 6 shows lines of constant phase for the inertial waves at three different values of the rotation rate Ω. The patterns on these three visualizations strikingly resemble those that are visible on a photograph in the experiment by McEwan (figure 7). The theoretical and measured angles in the simulations are shown in table 2.

The comparison in table 2 shows that measured angles are in good agreement with the dispersion relation and thus confirm the nature of the waves. It also constitutes an assessment of the validity of the numerical scheme we use, as far as the linear terms in the equations are concerned. We also observe that reflections at the walls

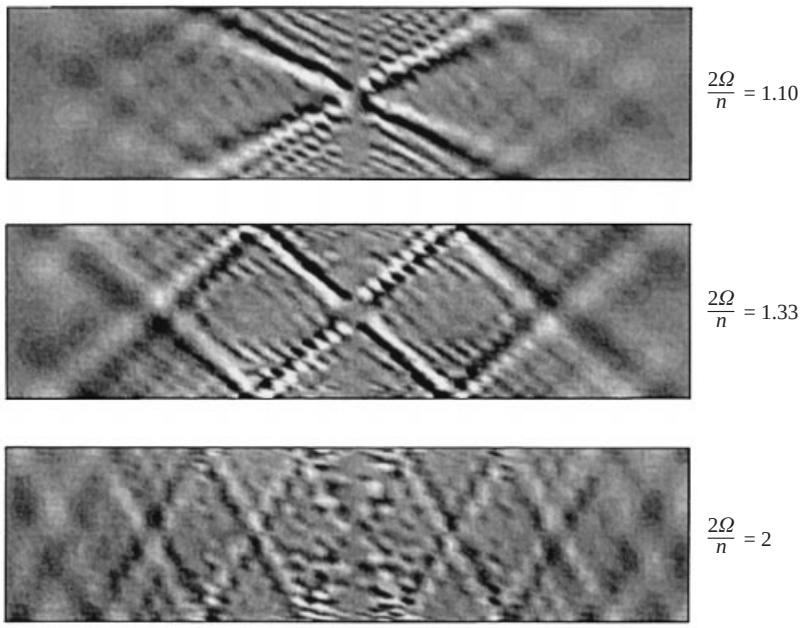

FIGURE 6. Two-dimensional plot of the lines of constant phase for the inertial waves (the wavevector is orthogonal to these lines).

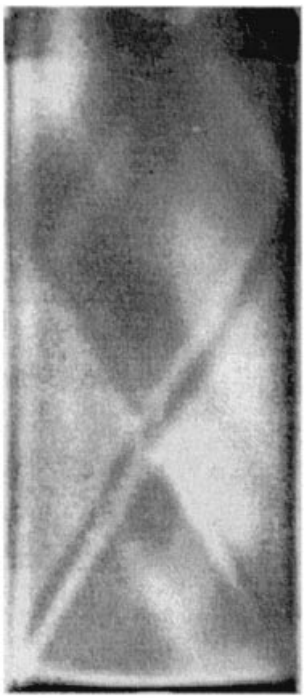

FIGURE 7. Photograph in the experiment by McEwan (1970). The tank is cylindrical, with its axis aligned to the axis of rotation.

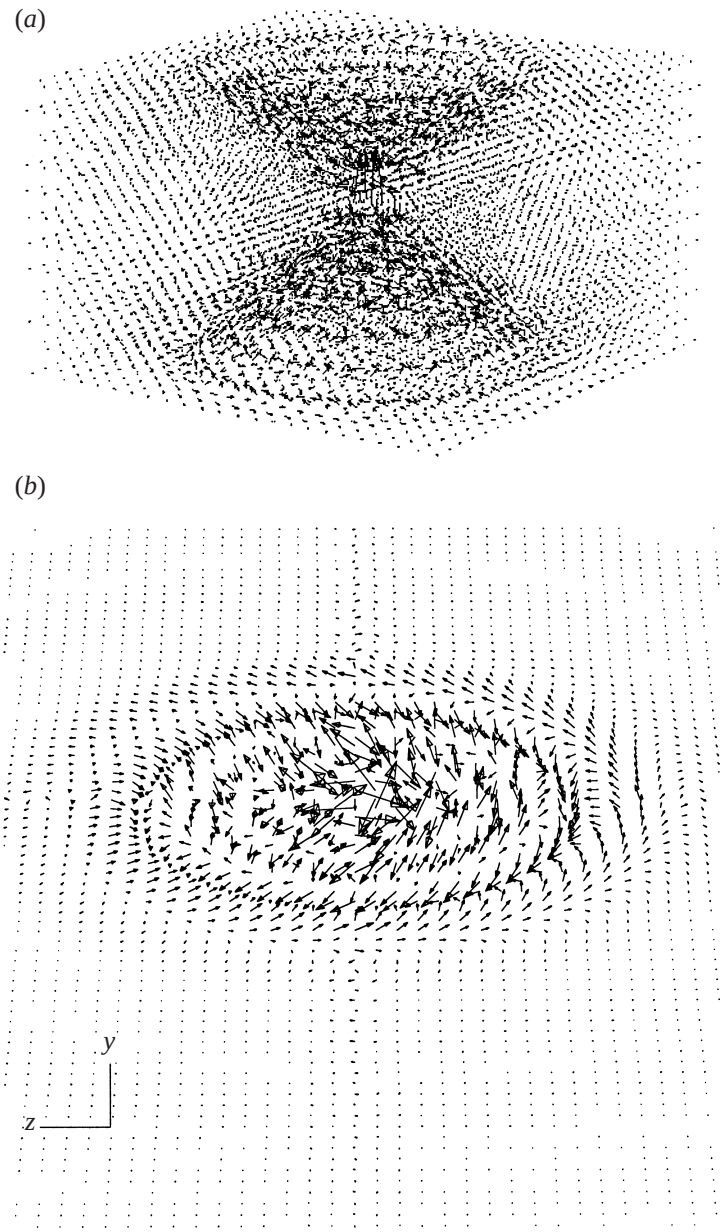

FIGURE 8. (*a*) Three-dimensional plot of the velocity field in the case $2\Omega/n = 1.33$. (*b*) Closer view of the velocity field in a (y, z)-plane away from the grid. The rotation of the velocity vector (phase change) can be observed along the radial directions.

are symmetric (with the angle of the incoming wave equal to that of the reflected one), as can be predicted from the fact that the rotation vector is orthogonal to the walls. Thus, there is no transfer of energy between wavenumbers by the reflection mechanism. The three-dimensional plot on figure 8(*a*) shows that the energy of the wave lies mainly on a cone. A closer view of the velocity field in a horizontal section of this cone, in the upper region, is shown on figure 8(*b*). It can be observed that the phase of the velocity vector is constant over each circle, whereas it rotates when

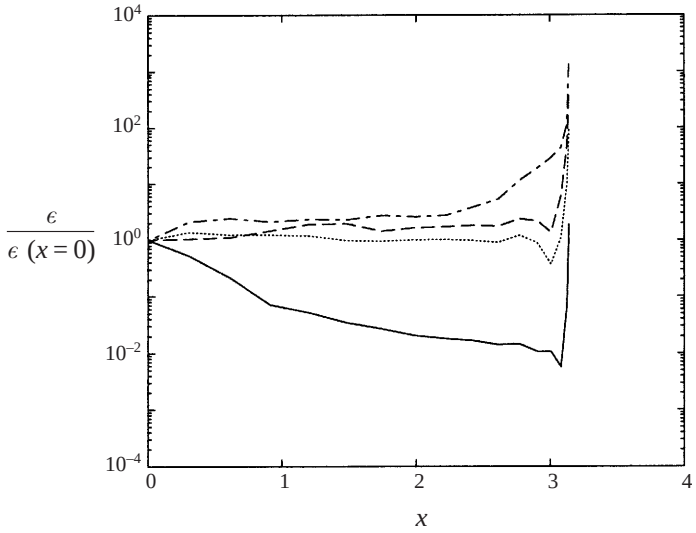

FIGURE 9. Dissipation profiles from the source to the upper wall for the inertial waves. —— , $\Omega = 0$; · · · · , $\Omega = 1.103$; — — , $\Omega = 1.33$; · — · , $\Omega = 2.00$.

moving away from the central axis. Note also that the core region is subjected to more random motion, as a remnant of the forcing used for generating the waves. Another interesting feature to notice is that the presence of the inertial waves, and their interaction with the wall boundary layer, induces extra dissipation, as illustrated on figure 9. Indeed, the larger the rotation rate, the closer to the vertical the wave direction is. Therefore, the number of reflections on the walls depends on the rotation rate, as can be checked on figure 6. Figure 9 also shows that the dissipation is largest in the case $2\Omega/n = 2$, which is also the case where more dissipation occurs at the walls. These plots do not tell us whether the dissipation is related directly to the rotation rate, but merely show that reflection of inertial waves is a dissipative process.

5. Freely decaying turbulence

We take here freely decaying turbulence, with or without rotation, and consider both the homogeneous case, and the inhomogeneous one with plane walls. The presence of solid boundaries can be important in the generation of anisotropy: indeed, many studies have shown that rotation can create anisotropy in initially isotropic homogeneous fields, but without visible evidence of a structuring; on the other hand, walls certainly play a role by means of Ekman pumping, even though this effect is counteracting the two-dimensionalization trend directly due to solid body rotation. Our numerical simulations are run with and without rotation, and in confined and fully homogeneous cases, aiming at isolating the effect of the walls on the structuration of the flow.

The homogeneous simulations are performed using a standard pseudo-spectral code with periodic conditions in all three directions, the Coriolis force being treated in an explicit manner (Rogallo 1981; Bartello, Métais & Lesieur 1994).

5.1. *Initialization method for the velocity field*

In the homogeneous case, let u_i be the velocity variable in physical space, whose spectral coefficients are

$$\hat{u}_i = \frac{1}{(2\pi)^3} \int_{\Re^3} u_i \, \mathrm{e}^{-\mathrm{i}\boldsymbol{k}\cdot\boldsymbol{x}} \, \mathrm{d}^3\boldsymbol{x}. \tag{5.1}$$

In order to get an initial velocity field, we use the method by Rogallo (1981) who defined two random components of the velocity field, in the plane orthogonal to $\boldsymbol{k}$, due to its divergenceless property. Therefore, by using a local frame of reference, whose unit vectors can be defined, say, as

$$\boldsymbol{e}^1(\boldsymbol{k}) = \frac{\boldsymbol{k}\times\boldsymbol{\Omega}}{|\boldsymbol{k}\times\boldsymbol{\Omega}|}, \quad \boldsymbol{e}^2(\boldsymbol{k}) = \frac{\boldsymbol{k}\times\boldsymbol{e}^1}{\boldsymbol{k}\times\boldsymbol{e}^1}, \tag{5.2}$$

$\hat{\boldsymbol{u}}$ then reads

$$\hat{\boldsymbol{u}} = \hat{\varphi}^1\boldsymbol{e}^1 + \hat{\varphi}^2\boldsymbol{e}^2. \tag{5.3}$$

The random amplitudes of each velocity components in this local frame are chosen as

$$\hat{\varphi}^1 = \sqrt{\frac{E(k)}{4\pi k^2}}\mathrm{e}^{\mathrm{i}\theta_1}\cos\alpha, \quad \hat{\varphi}^2 = \sqrt{\frac{E(k)}{4\pi k^2}}\mathrm{e}^{\mathrm{i}\theta_2}\sin\alpha. \tag{5.4}$$

At the initial time, α, θ_1 and θ_2 are picked in a random sequence with uniform distribution between 0 and 2π. The principle of this method is to construct a given distribution of the velocity field with zero triple correlations, but with double correlations specified through a given spectrum of kinetic energy $E(k)$. Indeed, $\hat{\varphi}^1$ and $\hat{\varphi}^2$ have to be such that

$$\int (\hat{\boldsymbol{u}}\cdot\hat{\boldsymbol{u}}^*)\,\mathrm{d}A(k) = E(k), \tag{5.5}$$

where $\mathrm{d}A(k)$ is a spherical shell of radius k and thickness $\mathrm{d}k$. Adjusted parameters include the energy in the spectrum, and the position of the peak of energy (alternatively the velocity r.m.s. value u and a given integral length scale). One thus obtains an incompressible velocity field which is also homogeneous isotropic. The phase α is the orientation of $\hat{\boldsymbol{u}}$ in the plane orthogonal to $\boldsymbol{k}$, whereas θ_1 and θ_2 are modified, from their initial value, by the phase scrambling induced by rotation. This same method is used for initializing the confined simulations, but an operation of re-projection of the resulting homogeneous random velocity field is performed, on the basis described in § 3.1.2, so that one gets a field which is compatible with the boundary conditions. The resulting loss of energy is small enough to be ignored.

5.2. *Parameters of the simulations*

The computational box is a cube of side 2π. The simulations resolution is 96^3 points. The spectral step (or minimum wavenumber) in the horizontal directions is $\Delta k = 1$, and the largest resolved wavenumber is $k_{\max} = 48$. We choose a given analytical spectrum for initializing the simulations (Orszag & Patterson 1972):

$$E(k,0) = \tfrac{1}{2}A_s\frac{u_0^2}{k_{peak}}\left(\frac{k}{k_{peak}}\right)^s \exp\left(-\tfrac{1}{2}s\left(\frac{k}{k_{peak}}\right)^2\right). \tag{5.6}$$

The parameter $s = 4$ is the slope of the spectrum at small wavenumbers. The peak of energy is placed at $k_{peak} = 9.5$ and the total initial energy in the box is $q^2/2 = 1.5$ (corresponding to a r.m.s. velocity $u_0 = 1$). Given the spectrum (5.6), the integral

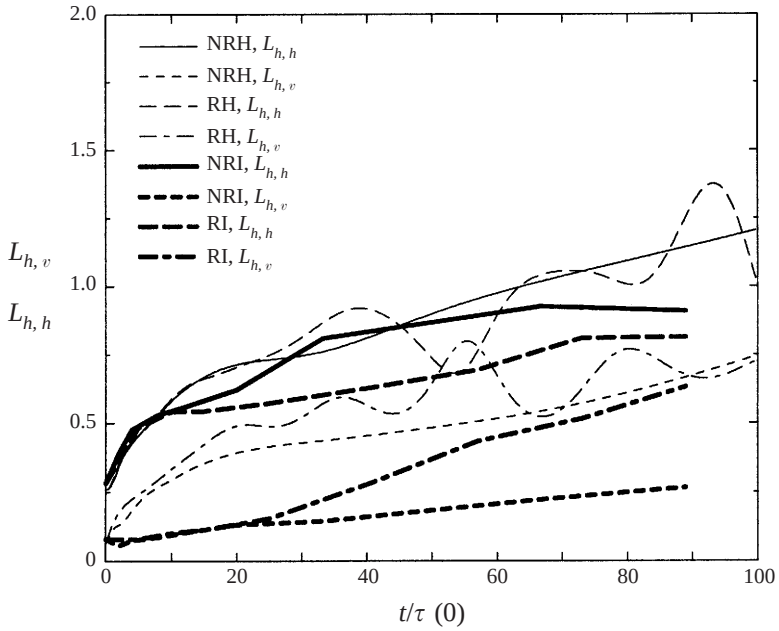

FIGURE 10. Evolution of the various directional integral length scales for the freely decaying simulations, both in the inhomogeneous (thick lines) and in the homogeneous (thin lines) cases, and with or without rotation.

	No walls (homogeneous)	With walls (inhomogeneous)
No rotation	NRH	NRI
With rotation	RH	RI

TABLE 3. Labelling of the different decaying turbulence runs.

length scale at the beginning of the computation can be obtained by the relation (see Batchelor 1953)

$$L_{f_0} = \frac{3\pi}{4} \frac{\int_0^\infty E(k)/k \, \mathrm{d}k}{\int_0^\infty E(k) \, \mathrm{d}k},$$

which gives $L_{f_0} = \sqrt{2\pi}/k_{peak} = 0.26$ (see figure 10) and amounts to 5% of the distance between the walls. No confinement effects are therefore felt by the flow at the beginning of the decay. Finally, the initial Reynolds number is

$$Re = \frac{u_0 L_{f_0}}{\nu}$$

with a given molecular viscosity ν. In all our simulations, we choose $\nu = 0.0025$, yielding an initial Reynolds number of 120.

In the following, computations will be labelled as shown in table 3. We have not performed here any pre-computation, as is sometimes done to allow the turbulent field to evolve to a more physical one, for we compare results from both wall-bounded and homogeneous simulations, which need to have as close initial conditions as

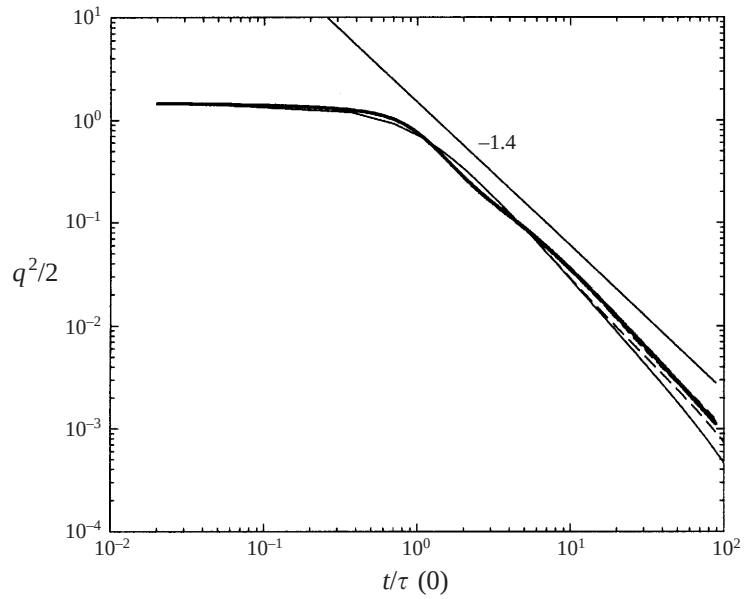

FIGURE 11. Evolution of the kinetic energy for the four freely decaying simulations.

possible. Initial pre-computations would provide a more realistic initial field, but with the drawback that statistical quantities of turbulence may already have evolved in a significantly different manner. This will allow us to analyse the effects of confinement by close comparison of both simulation situations. The initial conditions are therefore exactly prescribed by (5.6) in both computations. All the simulations have been performed over 90 eddy turnover times, which is the ratio $\tau(0) = L_{f_0}/u_0$ at $t = 0$, yielding the numerical value $\tau(0) = 0.3$.

The initial integral length scale based Rossby number is tuned approximately so that we anticipate that rotation should affect the flow dynamics after about 10 eddy turnover times, the flow being in a fully developped state at this time. Twice the rotation rate is $2\Omega = 0.3$, yielding $Ro^L = u_0/(2\Omega L_{f_0}) = 11$.

5.3. *Results of the simulations*

5.3.1. *Kinetic energy*

Figure 11 shows the evolution of the kinetic energy for the four simulations. This evolution is about the same in all four cases, indicating that the rotation has no significant effect on the energy cascade. The Reynolds number is too weak in the NRH and RH simulations to allow one to observe a discernible effect of rotation before the turbulence has lost too much energy to viscous dissipation. Indeed, figure 12 shows that the energy spectrum at $t/\tau(0) = 20$ exhibits a peak at $k = 2$. The decrease of the peak wavenumber towards the small values is expected and indicates the growth of the length scales in the flow. The peak cannot decrease any further, nor can the length scales grow; this demonstrates that the homogeneous computation is no longer realistic and physical after this time.

Let us also underline that the long-time behaviour of the length scale $L_{h,v}$ (figure 10) in the NRH simulation is strongly linked to the initial realization of the flow. Indeed, in the non-rotating case, turbulence decays faster, since the inhibiting effect of rotation on the energy transfer is not present. This limitation can be interpreted

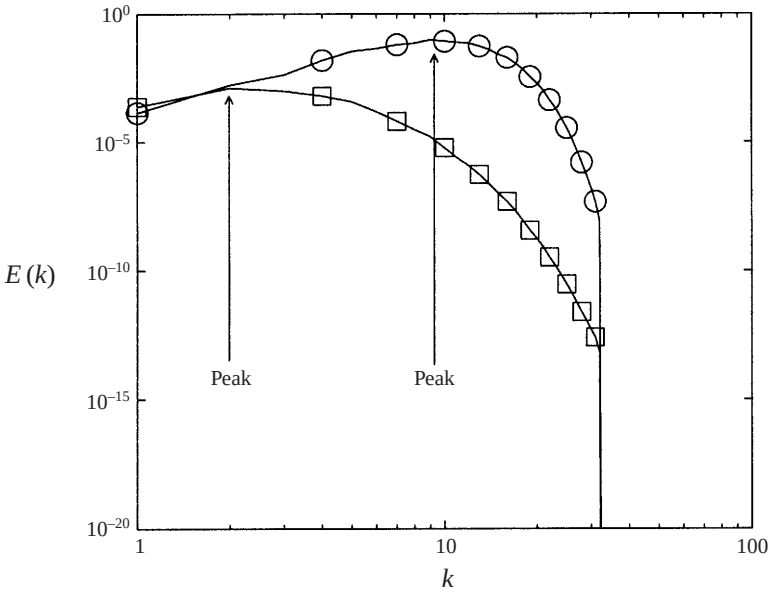

FIGURE 12. Three-dimensional energy spectra for run NRH at $t/\tau(0) = 0$ (circles) and $t/\tau(0) = 20$ (squares).

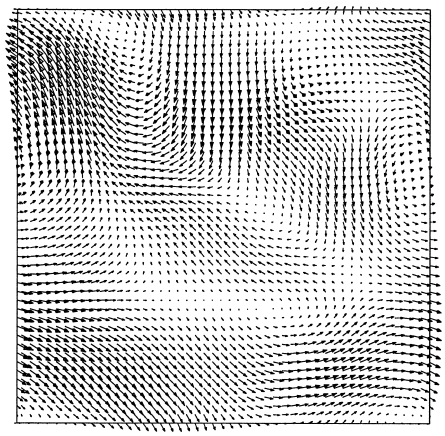

FIGURE 13. Velocity field in a plane of the simulation NRH at $t/\tau(0) = 20$, showing that only large-scale variability remains in the flow after such a long decay.

as a confinement of the turbulence scales by the size of the computational box. The mode $k = 1$ corresponds to a maximum wavelength (related to the size of the box), and $k = 2$ to half this length. This is well illustrated in the visualization of the velocity field of figure 13, at $t/\tau(0) = 20$, for the homogeneous computation. Note also that the integral length scales are then of the order of 0.75 (i.e. 12% of the box size). On the other hand, the inhomogeneous simulations can be pursued longer since the walls play an inhibiting role in the growth of the large scales. Figure 14 shows the velocity field for the NRI simulation at a much later instant than the homogeneous computation, since $t/\tau(0) \approx 90$. The turbulent structures are much more numerous and reasonably smaller with respect to the box dimension.

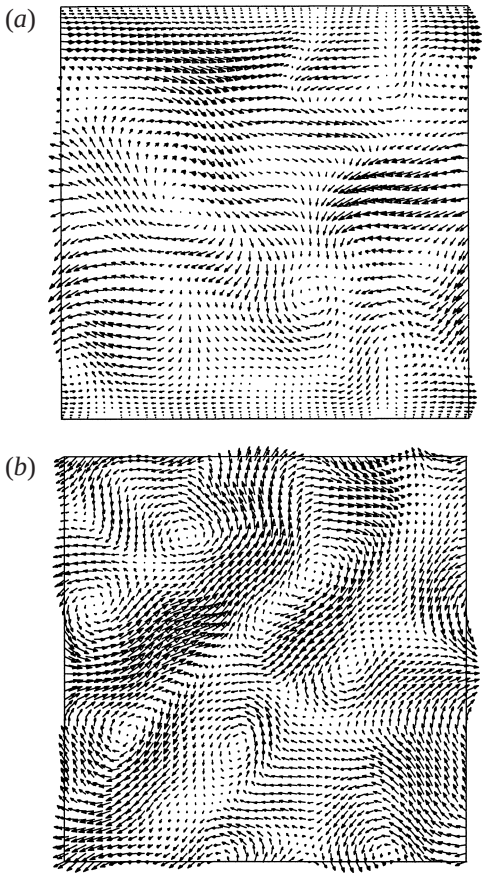

FIGURE 14. Velocity field for simulation NRI at $t/\tau(0) \approx 90$, (*a*) in an inhomogeneous (vertical) plane; (*b*) in a homogeneous (horizontal) plane.

5.3.2. *Skewness*

The evolution of the skewness is given on figure 15 for the first 8 eddy turnover times $\tau(0)$. The evolution of this quantity is in good agreement with that observed in homogeneous isotropic turbulence, even at low Reynolds number (see e.g. Tavoularis, Bennet & Corrsin 1978). Indeed, the skewness is always negative and begins to stabilize after 4 or 5 eddy turnover times, whence a fully developed turbulence state. This justifies the initial value of the Rossby number (≈ 11) for the rotating computations, since rotation does not have much effect during the period in which the triple correlations build up (the Rossby number reaches a value of 4 when the skewness is stabilized). The difference between S_v and S_h (see definition (3.13)), is of course non-existent in homogeneous isotropic turbulence. The lower absolute value of S_v may be explained by the limitation of vortex stretching in the direction orthogonal to the walls.

5.3.3. *Integral length scales*

The growth of vertical integral length scales due to rotation has already been identified in previous works, e.g. by Bardina *et al.* (1985) for homogeneous flows, and our homogeneous simulations with rotation lead to the same integral length scale separation. Regarding the simulations without rotation, NRH and NRI, we see

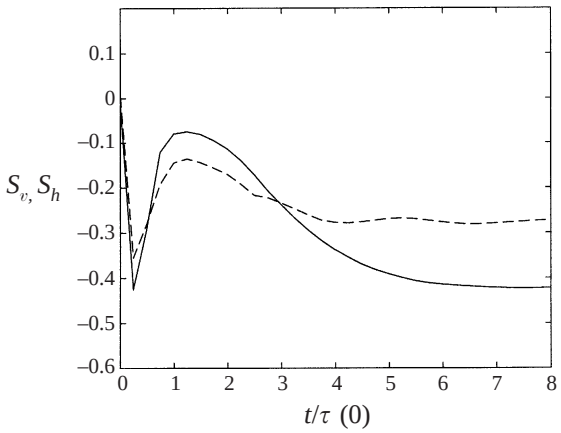

FIGURE 15. Evolution of the velocity-derivative skewness over the first eight eddy turnover times. —— , S_h; – – , S_v.

on figure 10 that the walls induce a different behaviour for the length scales $L_{h,h}$ and $L_{h,v}$. After a first short period of growth, due to the development of turbulence, of about 10 eddy turnover times, in both the inhomogeneous and homogeneous cases $L_{h,h}$ grows at an almost constant pace. Whereas in the homogeneous case no obvious effect of rotation is observed on this length, $L_{h,h}$ has a smaller value in the inhomogeneous rotating run RI than in run NRI. The length $L_{h,v}$ presents much more marked differences. First, in the wall-bounded case, it does not increase at the beginning as in the homogeneous case, indicating a strong confinement effect of the boundaries in the vertical direction. A modification of the growth of $L_{h,v}$ by rotation is seen at about $t/\tau(0) = 20$, remarkably when $Ro^v \simeq 1$, in both the homogeneous and the inhomogeneous cases. The trend is the same, since it appears that rotation increases $L_{h,v}$ with respect to the non-rotating case, a clue to vertically elongated structures in the flow.

5.3.4. *Anisotropy* b_{11}

The evolution of the anisotropy of the Reynolds stress tensor, b_{11}, is presented on figure 16 for runs NRI, RI and RH. In isotropic turbulence, b_{11} is of course zero. In the case of homogeneous turbulence subjected to rotation, this indicator is slightly positive, denoting the preponderance of the vertical component of velocity over the horizontal ones. In runs NRI and RI it is always negative. Without rotation, b_{11} reaches its smaller algebraic value, showing the damping of the vertical motion by the horizontal boundaries. In the rotating case, the evolution of b_{11} shows that the vertical components become stronger under the combined effect of rotation (as in the homogeneous case) and Ekman pumping. Rotation, associated with the action of the walls, thus creates an effect that competes with the damping of the vertical component by these very boundaries. The Ekman pumping phenomenon produces the vertical velocity component.

5.3.5. *Spectra*

Figure 17 shows that the spectra of turbulence and dissipation evolve quite fast to a developed state. After 2 eddy turnover times, the energy spectrum exhibits a $-\frac{5}{3}$ slope which was not present initially of course, due to the choice of the initial condition (figure 17*a*). It is worth noticing that after 2 eddy turnover times, the

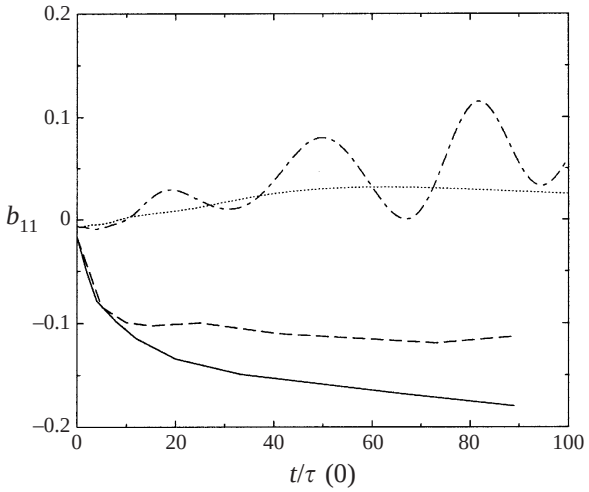

FIGURE 16. Evolution of the Reynolds stress tensor anisotropy component b_{11}: —, run NRI; — —, RI; · · · ·, NRH; · — ·, RH.

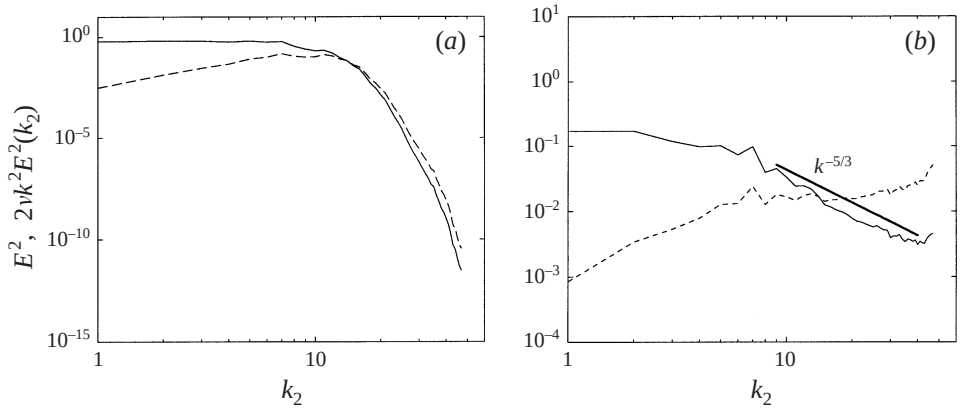

FIGURE 17. One dimensional spectra of: —, kinetic energy, and — —, dissipation, following the generation of the turbulent field by Rogallo's method. (*a*) $t = 0$; (*b*) $t = 2\tau(0)$.

dissipation is not very well resolved (location of the peak of the spectrum $2\nu k^2 E^2(k)$ on figure 17*b*). However, the following evolution of the computation shows that this lack of resolution does not influence the quality of the results, so that we can keep the advantage of having a rather high initial Reynolds number.

5.3.6. *Rossby number*

To characterize the structuring of rotating homogeneous turbulence, Cambon *et al.* (1997), define two macro Rossby numbers, based on vertical or horizontal velocity and length scales:

$$Ro^v = u_1/(2\Omega L_{11,1}) \quad \text{and} \quad Ro^h = u_2/(4\Omega L_{22,1}),$$

which are identical in isotropic homogeneous turbulence. The most useful one is Ro^v, in agreement with Jacquin's discussion in his experimental study. Accordingly, we show the evolution of the Rossby number Ro^v for the inhomogeneous run on

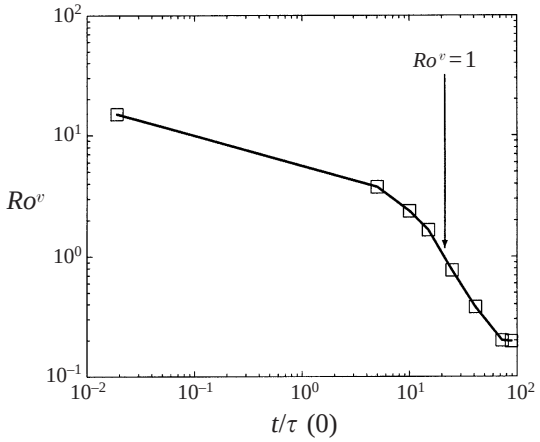

FIGURE 18. Evolution of the Rossby number Ro^v in the decaying case RI.

figure 18. At high Reynolds number, we recall that the analysis of the effect of rotation needs two Rossby numbers. One is based on the integral length scale and the other on the Taylor microscale. In our case, the Reynolds number is weak and these Rossby numbers are similar, since the ratio Ro^v/Ro^ω is proportional to $L/\lambda \propto \sqrt{Re}$ when the Reynolds number is large enough. We can however notice that differences in behaviour of statistical quantities between runs NRI and RI all appear when the Rossby number Ro^v is close to the critical unit value. Indeed, apart from the evolution of the horizontal length scales that begin to depart from each other when the Rossby number reaches 2, the rotating and non-rotating computations exhibit different evolutions of $L_{h,v}$ and b_{11} a bit later, when $Ro^v \approx 1$. The mechanisms of nonlinear transfer of energy are weak, and the departure of the length-scale anisotropy and of the velocity components may be put down also to wall effects rather than the mere effect of rotation. Even if the value of the critical Rossby number found here reminds one of the beginning of the transition zone found in homogeneous rotating turbulence (see figure 2), surely this critical value depends strongly on the confinement of the flow in between the walls. Therefore, before concluding too straightforwardly that this anisotropization mechanism is of same nature as that observed in high Reynolds number homogeneous turbulence, one has to quantify the two main effects of the solid boundaries on the evolution of the flow. First, if one computes an Ekman number based on the wall distance, one gets an indication of the strength of the confinement. This number $E = \nu/(\Omega L_1^2)$, can be seen as the square of the ratio between the thickness of the Ekman layer $\delta_E = \sqrt{\nu/\Omega}$ and the half-wall distance L_1. In our case, $E \approx 1.7 \times 10^{-3}$, which gives δ_E of the order of 2% of the wall distance $2L_1$. The extent of the Ekman layer is therefore small, and its effect negligible in the dynamics of turbulence. Second, we discuss the Ekman pumping mechanism in the next section.

5.3.7. *Ekman pumping*

Rotation plays a role through the presence of walls in run RI, by means of Ekman pumping. In order to confirm the existence of this phenomenon in the simulation, the correlation between the vertical components of velocity and vorticity is examined. In order to get correlations over each plane, and avoid the vertical variation of their

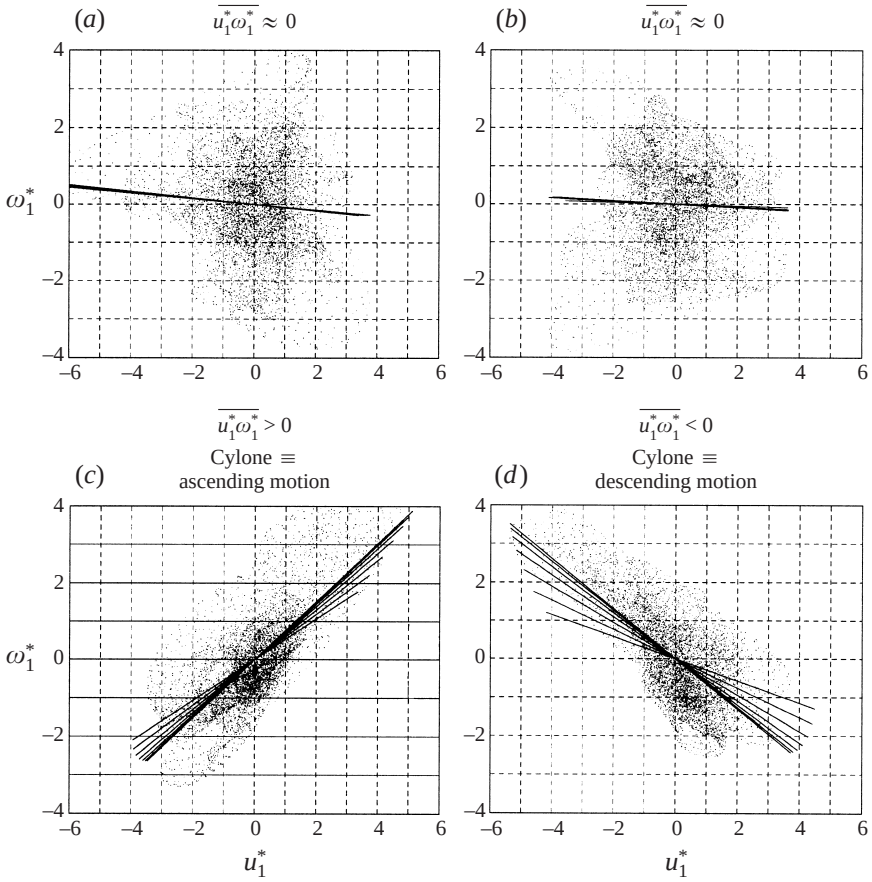

FIGURE 19. Correlation between vertical components of velocity and vorticity: (*a*) close to the bottom wall for run NRI; (*b*) close to the upper wall for run NRI; (*c*) close to the bottom wall for run RI; (*d*) close to the upper wall for run RI.

r.m.s. values, u_1 and ω_1 are non-dimensionalized by mean values of the velocity and vorticity in horizontal planes, namely u_1^* and ω_1^*.

Figure 19 shows these correlations for runs NRI and RI at $t/\tau(0) = 90$. Even though the turbulence is rather weak at this time, the plots confirm the combined action of rotation and the wall in the form of Ekman pumping. The graphs are plotted in the seven planes closest to the walls, the farthest one being at 5% of the box size away from the wall (the Ekman layer thickness has been estimated at 2% of the wall distance). Regarding the non-rotating case, NRI, it is clear (see figures 19*a* and 19*b*) that u_1^* and ω_1^* are uncorrelated and that we indeed have $\overline{u_1\omega_1} \approx 0$. A strong correlation is clear on figures 19(*c*) and 19(*d*), indicating the action of Ekman pumping. For instance, we have $\overline{u_1\omega_1} > 1$ close to the lower wall. This is in agreement with Ekman pumping since positive components of vertical vorticity (cyclonic in our notation) are associated with ascending motion, and vice versa. It is of course the other way round for correlations obtained close to the upper wall, where, in turn, we have $\overline{u_1\omega_1} < 1$.

Note that the least-squares lines on figures 19(*c*) and 19(*d*), have decreasing slopes when moving away from the walls; this indicates the decreasing effect of the pumping at large distances from the solid boundary. Note also that there is a net production

of helicity $\langle \boldsymbol{u} \cdot \boldsymbol{\omega} \rangle$ by Ekman pumping close to a wall, whereas this quantity can never be created by rotation in homogeneous turbulence.

These results constitute a fundamental difference with those obtained in the homogeneous case where coherent structures may not be visible, even if there exists anisotropy in the integral length scales. Here, even at weak Reynolds number, and at an instant when turbulence is almost extinguished, the Ekman pumping is active and produces vortex structures with axes parallel to the rotation vector.

6. Confined forced rotating turbulence

The study of the characteristics of turbulence without mean motion is very important for fundamental analyses. Turbulent transport may then be produced by inhomogeneities in the flow; for instance, when two layers of different turbulent intensities, in terms of r.m.s. velocity values and integral length scales, are adjacent. Such self-convected turbulence is said to be *diffusive*. Diffusive turbulence may be produced by various experimental means, leading to different flow characteristics, especially regarding the isotropy of the layer created in the vicinity of the generating apparatus. Some related work is described hereafter.

6.1. *Review of diffusive turbulence work*

In order to set up an experimental apparatus and methods for measuring turbulence in water, using hot wire probe, Bouvard & Dumas (1967) have built a 'turbulence tank' with square section in which a perforated plaque oscillates vertically. In view of the high interest in obtaining vertical variations of the r.m.s. of the fluctuating velocity, they have looked for a theoretical explanation of their results. The basis of reasoning is that at each level, the motion is statistically stationary and results from the equilibrium between the input of turbulent kinetic energy by diffusion from the bottom of the tank, and its destruction by molecular viscosity, the turbulence being assumed to remain isotropic. By introducing a diffusion coefficient, and despite the crudeness of the hypotheses, the theoretical result is in strikingly good agreement with the experiments. The latter were conducted using a perforated plaque, but it appears that the characteristics of the turbulence generating device influence strongly the fluctuating quantities. Thompson & Turner (1975), have performed experiments whose goal was to find the relation of different spatial profiles with the frequency and amplitude of the grid; they also find a dependence upon the shape of the rods the grid is made of. An $x^{-1.5}$ power law, where x is the distance from the grid, is found for the decrease of the r.m.s. quantities and a linear growth for the integral length scales. The r.m.s. values are proportional to the excitation frequency in the case of square section rods. Hopfinger & Toly (1976), used the same experimental setting as Bouvard & Dumas (1967), replacing the perforated plaque with a square rod grid. They tried to find the influence of each of the characteristic parameters of the grid, including the mesh size; the frequency f, mesh size M and stroke S are called external parameters. The linear dependence of the r.m.s. quantities on the frequency, as proposed by Thompson & Turner (1975), is confirmed, and the authors propose the following general form:

$$\frac{u}{fS} = CS^{1/2}M^{1/2}x^{-1}.$$

Since the turbulence is anisotropic, De Silva & Fernando (1994) have considered this same form again, but distinguishing the u_0 – vertical – and v_0 – horizontal – velocity

components (the zero index refers to properties of *stationary* turbulence):

$$u_0 = C_2 S^{3/2} M^{1/2} f x^{-1},$$

$$v_0 = C_1 S^{3/2} M^{1/2} f x^{-1},$$

$$l_0 = C_3 x,$$

where f is in Hz, $C_1 \approx 0.22$, $C_2 \approx 0.26$ and $C_3 \approx 0.10$. The length l_0 is the integral scale of turbulence. These constants have to be adjusted depending on the geometry of the grid and the shape of the rods. Note that the Reynolds number based on u_0 and l_0 is uniform in the turbulent layer. McDougall (1979) studied the relationship between the excitation frequency and the r.m.s. profiles. Using a device allowing tuning of the frequency continuously between 1 Hz and 10 Hz, he shows that the linear dependence found by Thompson & Turner (1975) and Hopfinger & Toly (1976) is no longer valid above a given value of the excitation frequency (7 Hz). More recently, Drayton (1993) has re-done the experimental study on an oscillating grid, but adding a Lagrangian point of view to the previous Eulerian one. Let us also quote the theoretical work by Long (1978), who constructs a model that agrees quite well with the various experimental observations, with respect to the linear growth of the integral length scales and the decay of the r.m.s. velocity as x^{-1}.

All these experiments have recently been complemented by numerical ones. Using direct numerical simulations with periodic conditions in the three directions, Briggs *et al.* (1996) have studied the mixing layer without mean shear or rotation. The mixing layer is a region between two turbulent layers of different turbulent kinetic energy intensities. The most energetic one is forced by injecting energy at a given frequency, by remote analogy with an actual oscillating grid. We notice that the r.m.s. velocity decreases as $x^{-1.35}$.

We now provide details about the experiment by HBG who observe a modified behaviour of the flow when placing the whole previous experimental apparatus on a turntable.

6.2. *Oscillating grid turbulence with rotation*

The experimental apparatus of HBG is as follows. A cylinder of 40 cm diameter and 80 cm depth is made out of transparent material. It contains an oscillating grid system whose mean position is located 15 cm above the bottom. The whole installation is subjected to solid body rotation. The grid has 1 cm section rods, 5 cm apart. The amplitude A of the oscillation and its time frequency n can be changed over a wide range (up to 20 rad s^{-1} for n and 5 cm for the stroke S, which is twice the grid amplitude).

Hopfinger & Toly (1976) define the fluctuating velocity and integral length scale as

$$u_{\text{r.m.s.}} = \frac{K_1 n}{x}, \qquad l = K_2 x. \tag{6.1}$$

The amplitude is fixed to 4 cm and, for this value, since K_1 and K_2 depend on it, they find

$$K_1 = 0.83\,\text{cm}^2, \quad K_2 = 0.26. \tag{6.2}$$

A transparent top is placed on the tank in order to help visualizations and to avoid the undesirable β effect, which anyhow later on appeared to be negligible. Experiments are performed with different frequencies and rotation rates as enumerated in table 4.

n (rad s^{-1})	$3, 30 \times 2\pi,\ 6.63 \times 2\pi$
2Ω (rad s^{-1})	$0.2\pi,\ \pi,\ 2\pi,\ 20\pi$

TABLE 4. List of frequencies and rotation rates used in the experiment by HBG.

Characteristic velocity and length u and l are defined far away from the grid, so that the flow dynamics depends on five non-dimensional parameters:

Grid Rossby number	$Ro = n/2\Omega \approx 3$–33,
Reynolds number	$Re = ul/\nu \approx 10^3$,
Ekman number	$Ek = \nu/(2\Omega l^2) \approx 10^{-5}$,
Rossby number	$Ro^l = u/(2\Omega l) \approx 5 \times 10^{-2}$,
Aspect ratio	$H/l \approx 3$–6.

6.3. *Experimental observations*

The grid Rossby number is defined as $Ro = n/(2\Omega)$. Far enough from the grid, observations show a given number of vortices, mainly cyclonic, whereas no obvious organised structures are visible in the lower part. When the oscillating frequency increases, or equivalently when the rotation decreases – both leading to an increase of the grid Rossby number – anticyclonic vortices appear that tend to concentrate in an outer annulus in the tank. These vortices are less intense than the cyclonic ones. Such a transition appears at a given distance from the tank walls, still to be determined. In the region close to the grid, the flow is rather unaffected by rotation whereas it is dominated by the rotation away from the grid. A local Rossby number may then be defined as

$$Ro^l(x) = \frac{u(x)}{2\Omega l(x)}.$$

Considering the relations given by Hopfinger & Toly (1976) and assuming a constant transitional Rossby number, we get

$$Ro_T = \frac{u(x_T)}{2\Omega l(x_T)} = \frac{K_1}{K_2}\frac{n}{2\Omega}\frac{1}{x_T^2} = \text{constant}.$$

From the values of x_T for different rotation rates and given K_1 and K_2 from (6.2), one gets the following value for the transitional Rossby number:

$$Ro_T = 0.2.$$

This numerical value cannot directly be identified as that found in the case of homogeneous turbulence, since, on the one hand, our specific context is a confined forced flow, and on the other hand it corresponds to an *abrupt* structural transition, which is not visible in homogeneous turbulence.

6.4. *Numerical approach to the experiment*

Yang (1992) has recently performed a numerical simulation in a context close to the experiment by HBG. He uses a pseudo-spectral code with two homogeneous directions along which the flow is assumed to be periodic (Fourier decomposition), and an inhomogeneous direction along the rotation axis (Chebyshev mode decomposition). Such a simplified configuration cannot reproduce the lateral confinement effect as in the experiment, but allows boundary conditions on the top and bottom. It also does not require the spatial vertical periodicity of the forcing process as was the case

in the simulations by Briggs *et al.* (1996) using a three-dimensional Fourier code. In order to model the oscillating grid, Yang (1992) introduces a complicated local forcing aimed at generating isotropic turbulence with given energy level in a plane close to the bottom wall. This turbulent region corresponds to given time and length scales. Such a forcing procedure is justified from the experimental statement that turbulence generated by an oscillating grid is very much like isotropic turbulence, close to the grid. Although Yang's results were encouraging enough to suggest a follow-up of this work, his computations dramatically suffer from the coarse vertical resolution he had (only 17 spectral points), which constitutes a severe handicap as far as the statistical analysis is concerned; namely the evaluation of spatial decay laws for statistical quantities, and too low a Reynolds number, limited by the resolution. The forcing also has an important drawback, since it does not implicitly involve parameters related to the grid, such as the mesh size, amplitude and frequency of oscillations, whose major influence on the flow has been widely demonstrated in many experiments on oscillating grid turbulence – as discussed in § 6.1. The statistical analysis can be improved as well, by extending it to spectra and directional integral length scales, and the three-dimensional visualizations can be improved.

Using an analogous numerical simulation code, we have reproduced the same geometrical configuration, using a more 'physical' forcing that depends upon the above-mentioned grid parameters, and higher resolutions permitted by parallel computations with distributed computer memory. In order to reproduce the experiment with our numerical simulations, we solve system (3.1), including a forcing term $\boldsymbol{f}$ that does not derive from a potential. This term needs to contain spatial and temporal information as close to those of the oscillating grid as possible. The chosen shape of the forcing is a superposition of a deterministic function that explicitly contains the grid parameters (mesh size M, amplitude $S/2$ and time frequency n), and of a random component $\boldsymbol{\beta}$, which is a random variable with uniform distribution over an amplitude of order of 25% of S. Acting in the plane $x = x_g$ (g for grid), this term is

$$f_i(x_g, y, z, t) = \frac{n^2 S}{2}\left(\delta_{i1}\cos\left(\frac{2\pi}{M}y\right)\cos\left(\frac{2\pi}{M}z\right)\sin(nt)\right) + \beta_i. \tag{6.3}$$

Alternatively, this kind of forcing is also analogous to the experimental one used by Colin de Verdières (1980), with alternating sources and sinks. Apart from the lateral boundaries, we use a geometry close to that of the experimental apparatus in HBG. It is shown on figure 20. The complete system, with rotation, is characterized by seven parameters, namely the vertical dimension L_1, the horizontal one $L_2 = L_3$, the mesh size M, the stroke and time frequency of the grid, S and n, the kinematic viscosity ν and the rotation rate Ω. Given that we have two fundamental dimensions, a time and distance, we therefore need five non-dimensional numbers. Three of them come from purely geometrical considerations, the other two being the Reynolds and Rossby numbers, related to the dynamics of the flow. Choosing S and n as the reference length and time frequency scales, these numbers are defined as

$$Re = \frac{nS^2}{\nu} \quad \text{and} \quad Ro = \frac{n}{2\Omega}. \tag{6.4}$$

All the following quantities presented are non-dimensionalized with the help of the reference length S, and n. The simulations are performed using a numerical domain of size $13.4 \times 8 \times 8$ ($x \in [-6.7; 6.7]$, $y \in [0; 8]$, $z \in [0; 8]$) with a mesh size identical to the grid stroke (generally the case in most oscillating grid experiments). The forcing

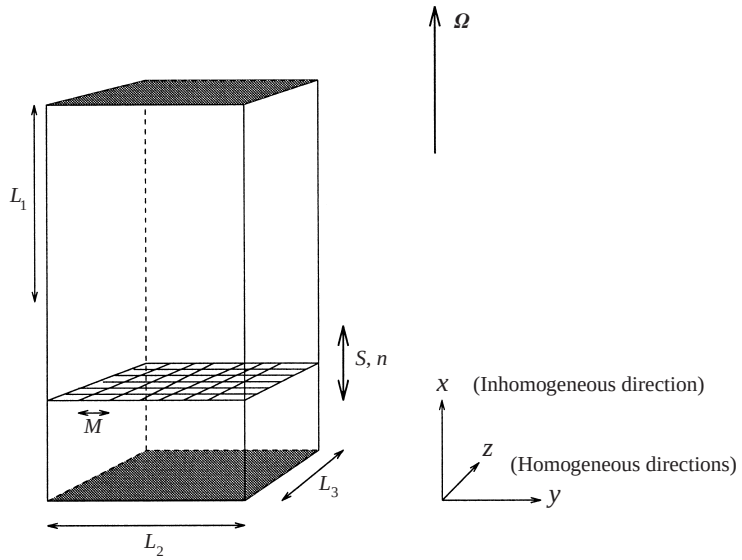

FIGURE 20. Schematic of the computational domain in the numerical experiment on rotating forced turbulence. The grid is located closer to the bottom wall, as in the experiment by HBG.

Run	*Ro*	*Re*	Resolution	No. of periods	Computer
SR	∞	1100	$96 \times 96 \times 96$	88	DEC server 8200
R50	50	10000	$96 \times 128 \times 128$	120	CRAY T3E
R20	20	1100	$96 \times 96 \times 96$	64	DEC server 8200
R3	3.32	1100	$96 \times 96 \times 96$	44	DEC server 8200
Yang ∞ to $1.63 \approx 170$			$17 \times 48 \times 48$	10	—

TABLE 5. Parameters of the simulations with forcing.

plane is located at $x_g = -3.35$, and we shall denote $x' = x - x_g$ the abscissa with respect to the forcing plane.

Simulations are referenced as shown in table 5, depending on the Reynolds and Rossby numbers. Runs SR, R20 and R3 have been done on the sequential computer DEC8200 at LMFA. Each iteration needs 30 CPU s, leading to total durations of the runs from ten to a hundred hours. Run R50, at higher resolution, was done on the Cray T3E of IDRIS.

The Reynolds number computed as $Re = ul/\nu$ was of the order of 10^3 in the experiment by HBG. In our simulations, it is much smaller, of the order of $Re \sim 20$, due to the fast decrease of energy away from the grid, at which $Re \sim 100$. We shall see in the following results that this low value does not affect the good qualitative agreement of the simulations with the laboratory results.

The simulations start from fluid at rest in the rotating frame. The total energy grows and stabilizes quickly (within two or three periods of forcing), but the statistical stationary state is not reached at this time. The integral length scales, and more specifically $L_{11,1}$, evolve on a slower basis. We thus choose to assume that the statistical stationary state is reached when this length scale is stabilized. Looking at $L_{11,1}$ in time shows that it is necessary to evolve over 50 grid periods, making it 15 times the required convergence time for energy.

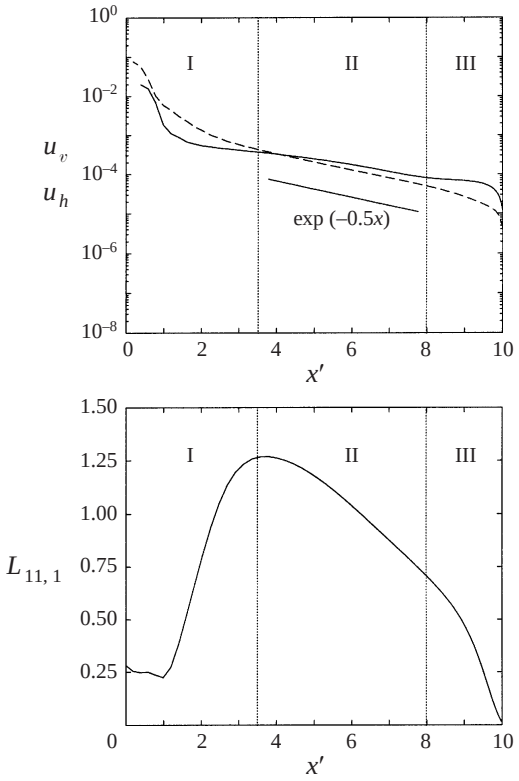

FIGURE 21. Spatial evolution of mean profiles of the length scale $L_{11,1}$ and of the r.m.s. velocity components, in the forced non-rotating case.

The same length scales as in the previous section for freely decaying turbulence are studied, namely $L_{h,h}$ and $L_{h,v}$. They are useful in providing information on the spatial coherence in the horizontal and vertical directions respectively. The spatial variations of the kinetic energy, and of the r.m.s. velocity are also studied, as well as the evolution of the Rossby number.

6.5. *Non-rotating case*

The non-rotating simulation is a pre-requisite to the rotating simulations, which allows one to estimate the level of energy in the forcing plane and the behaviour of the r.m.s. velocity and length scales in the case of pure diffusive turbulence. It also provides valuable information on the evolution of these quantities. Figure 21 shows both the r.m.s. components $u_v = u_1$ and $u_h = (u_2 + u_3)/2$, and the length $L_{11,1}$ profiles. Their behaviours are linked, for it is possible to identify three zones in the domain. In the first one, labelled (I), the velocity decreases following a power law, while $L_{11,1}$ increases. However the exponent of decrease of kinetic energy is found to be quite different from the one observed experimentally in diffusive turbulence. In zone (III), the components of the velocity, as well as the integral length scale, decrease to zero when approaching the wall. The intermediate zone (II) is more interesting. From $x' = 4$ to 8, say, we notice an exponential decrease of the energy, while $L_{11,1}$ decreases. We can explain this behaviour with the following simple argument.

In the case of high enough Reynolds number diffusive turbulence, Thompson & Turner (1975) propose (see also Batchelor 1953)

$$\mathrm{d}(u^3)/\mathrm{d}x = -Bu^3/l, \tag{6.5}$$

where B is of the order of unity. In that case, energy decreases spatially by *inertial* dissipation, since the terms $-Au^3/l$ or $-Bu^3/l$ can be interpreted as the action of an eddy viscosity ul on a shear u/l (with $-u^3/l = -ul(u/l)^2$). Experiments on oscillating grids have shown that the scale of these structures increases away from the grid, and that energy decreases following a power law. This is retrieved here by stating that $l = \beta x$. We then get the evolution equation for u in the form

$$u = u_0(x/x_0)^{-B/3\beta}. \tag{6.6}$$

Keeping constant the length scale of the flow, $l = \alpha =$ constant, the spatial evolution law becomes

$$u = u_0 \mathrm{e}^{-B/3\alpha(x-x_0)}. \tag{6.7}$$

Although equation (6.5) is obtained at high Reynolds number, the spatial evolution of $L_{11,1}$ and of the energy are closely related. The blocking of the integral length scale seems therefore to be responsible for this behaviour, in agreement with experimental results by Risso (1994).

Other lengths, specifically with horizontal separation, behave strangely with respect to the usual behaviour in diffusive turbulence: no evident increasing or decreasing trend may be seen. The weak Reynolds number, the random part of the forcing, and the limited propagation distance away from the grid, due to the presence of walls (that also perturbate the computation of the lengths), are certainly to blame for this phenomenon. However, we shall see that these scales evolve consistently in the rotating computations, with a growth of the lengths with vertical separation, and a decrease of those at horizontal separation.

6.6. *Rotating case*

Decaying simulations in § 5 have brought to light an important effect of rotation due to the action of walls, with the appearance of vortex structures in the wall region. The present simulations are devoted to studying the combined effect of rotation, confinement and local forcing, in order to identify long lasting vortex structures aligned with the rotation axis. Their presence is suggested by the particular behaviour of the various statistical quantities and eventually confirmed by visualizations. From a statistical point of view, attention will be more specifically dedicated to study the transitional Rossby number between the region close to the grid and the far region.

6.6.1. *Reynolds and Rossby numbers*

The validity of the rotating simulations depends on the Rossby and Reynolds numbers in the flow. We have indeed noticed that these two parameters play a role in the number and size of the organised structures created by the Coriolis force. Therefore, periodicity conditions in the homogeneous directions (orthogonal to the rotation axis) may interfere with the dynamics of the flow if these structures are too large. In order to pick the best rotation rates in the presented simulations, we have looked for a rough estimate of the number of structures depending on the Reynolds and Rossby numbers, using low-resolution computations ($48 \times 64 \times 64$).

The first four runs are performed using a constant Rossby number $Ro = 0.25$ and a variable Reynolds number, whereas the following four runs correspond to a constant

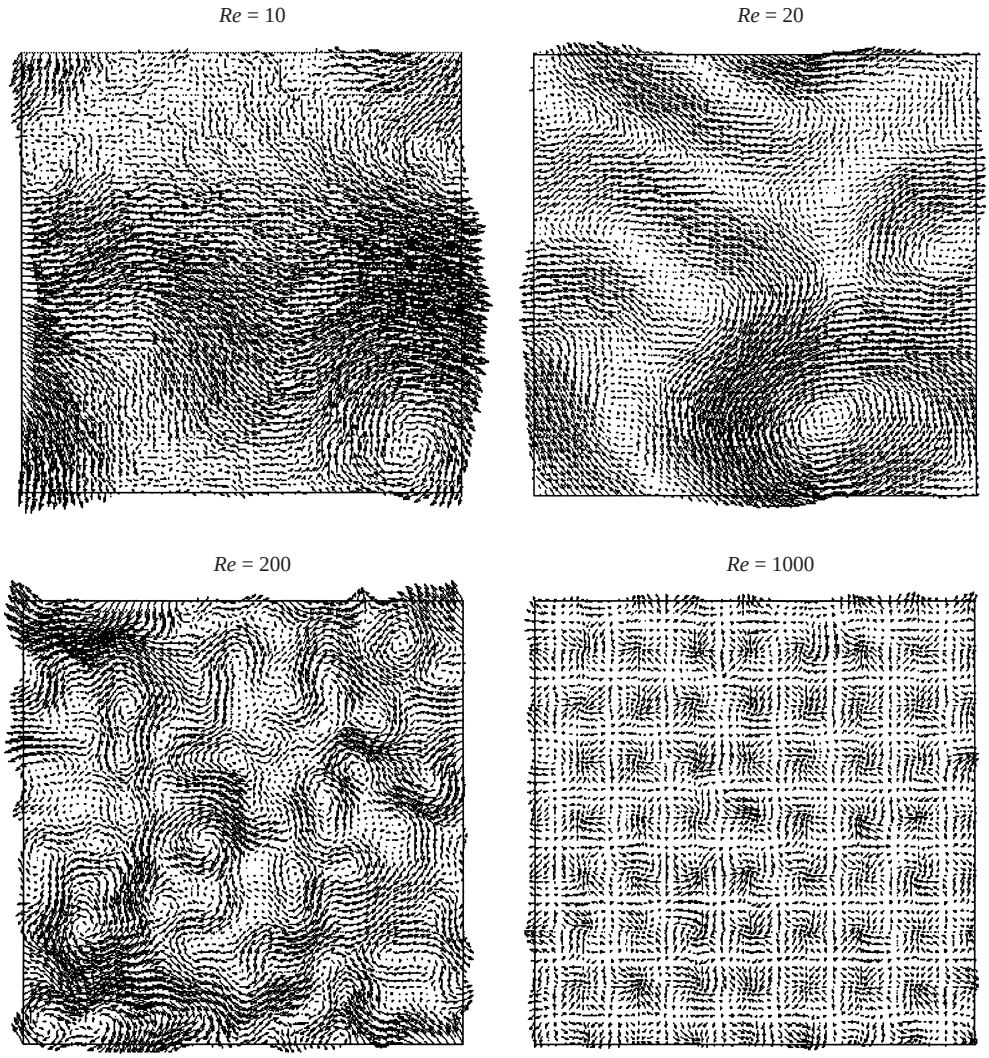

FIGURE 22. Plot of the velocity field at fixed Rossby number $Ro = 0.25$ with variable Reynolds number.

Reynolds number of $Re = 100$ and variable rotation rates. Figures 22 and 23 show the velocity fields obtained in a plane orthogonal to the rotation axis, away from the grid, and close to the upper wall. It is easy to see that the number of structures increases with the Reynolds number and increases with the rotation rate (or with the inverse of the Rossby number). The eight computations do not allow one to find accurately a simple functional relating the number of structures and the Reynolds and Rossby numbers. However, it seems that the population of vortices varies roughly like Re/Ro, i.e. the inverse of the Ekman number $Ek = Ro/Re$. HBG have noted in their experiment that the number of vortices and the inverse of the grid Rossby number are proportional. They have also observed a ratio 4.5 between the spacing of the vortices and their size, which is not found here because of the weakness of the Reynolds number. Indeed, in the moderate-resolution simulations, no isolated vortex appears, so that their size is roughly equal to their spacing.

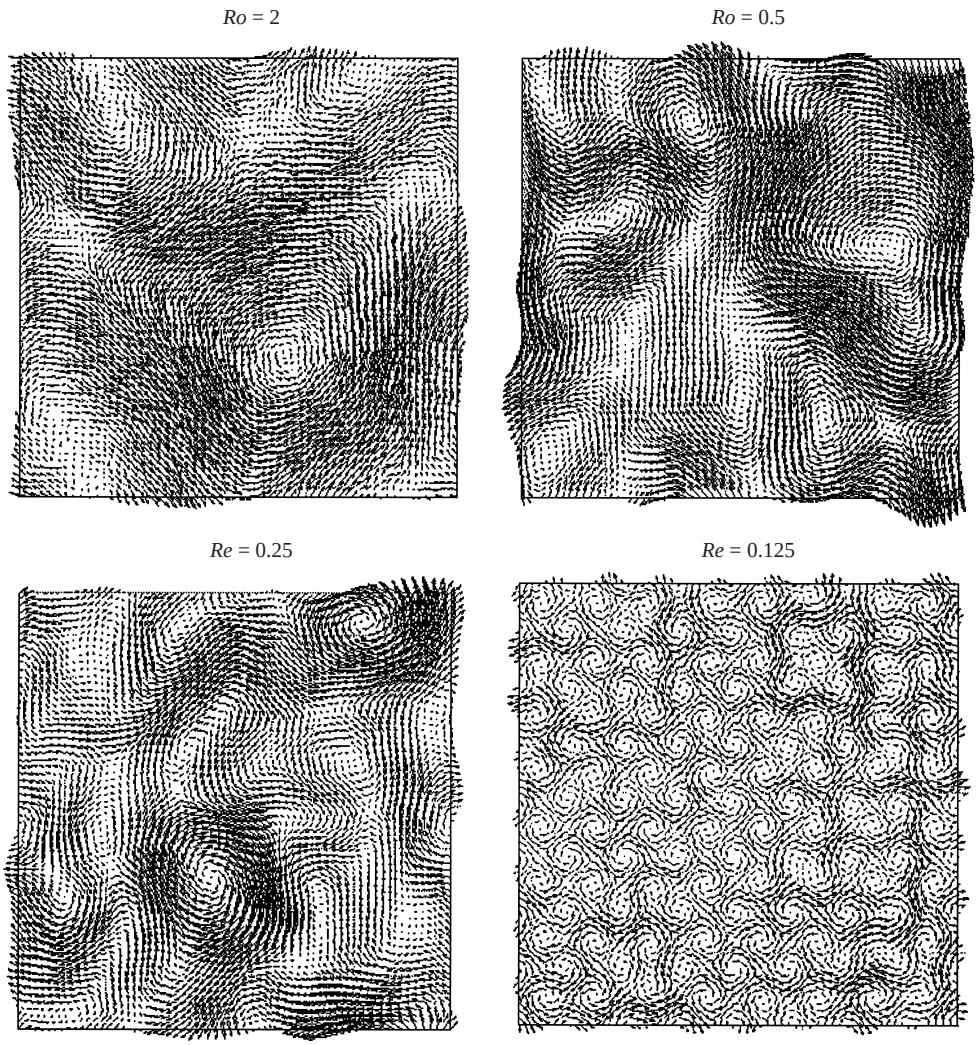

FIGURE 23. Plot of the velocity field at fixed Reynolds number $Re = 100$ and variable Rossby number.

Figure 24, showing velocity fields when the steady state is attained, confirms the relation between the number of vortices and the Rossby number in the physical and numerical experiments, and illustrates our last remark about the spacing of vortices, that the spacing and the size of the vortices are of the same order in the simulations.

6.6.2. *Statistical analysis*

In run R3, we use, as a reference, the weaker Rossby number in the HBG experiment, $Ro = 3$. The parameter 2Ω is therefore tuned to $\frac{1}{3} \approx 0.3$, which corresponds to a strong rotation rate. Upon looking at the results obtained in the non-rotating case, it appears that the r.m.s. velocity at the level of the grid is of the order of 0.1. The local Rossby number is therefore of the order of 0.3 at the grid. This domination of rotation automatically eliminates the possibility of having a region close to the grid where the flow would not be influenced by rotation. This computation can therefore not give us any information about an eventual 'structural' transition, as observed by

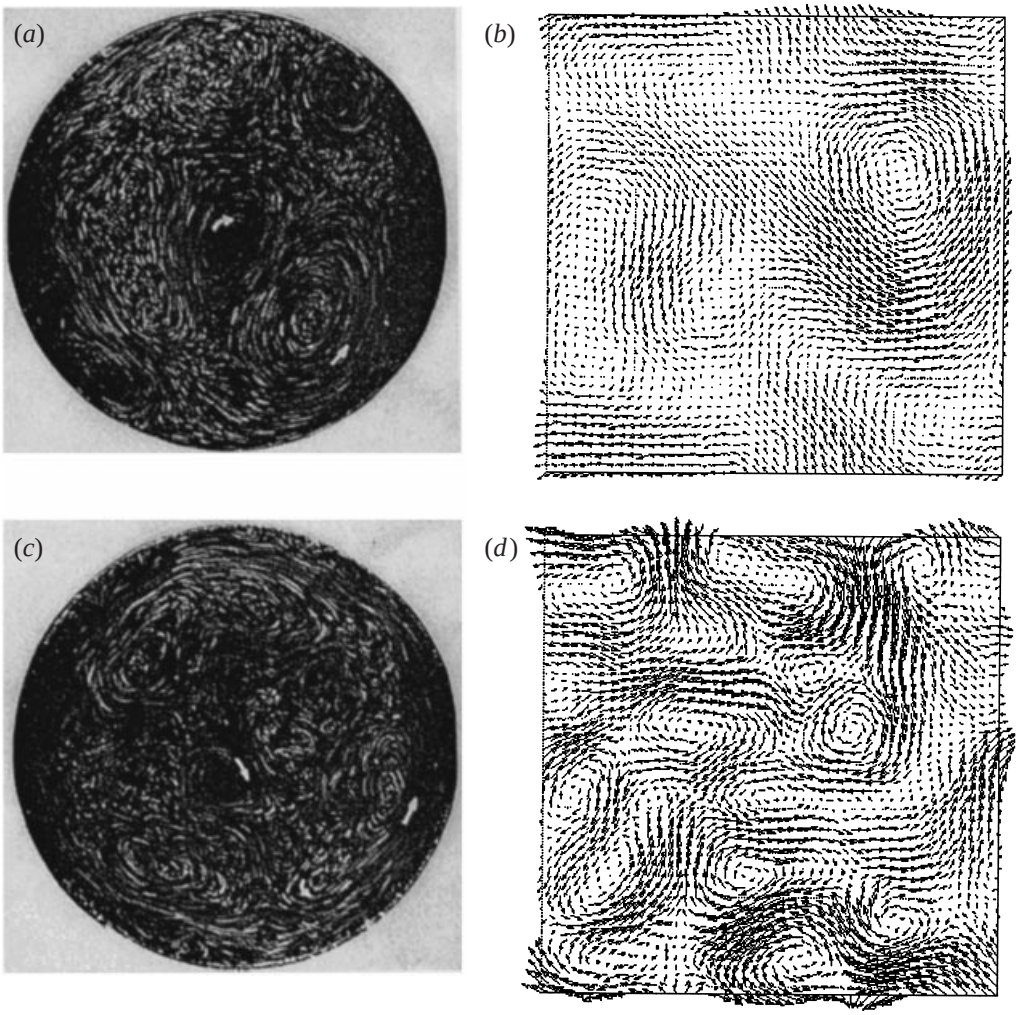

FIGURE 24. Qualitative comparisons between flow visualization in (*a*) the experiment by HBG at $Ro_G = 33.2$ and (*b*) the simulation at $Ro_G = 20$; (*c*) the same experiment at $Ro_G = 6.63$ and (*d*) the simulation at $Ro_G = 3$.

HBG. This constitutes the justification for performing runs R20 and R50, in view of the observations made in § 6.6.1.

Energetics

Regarding the spatial evolution of energy, the three runs SR, R20 and R3 exhibit an exponential decay, as found in the non-rotating case. However, the energy decay rate is lower at high rotation rate, which is in agreement with the generally observed reduction of energy transfer by rotation. Energy profiles are shown on figure 25(*a*). Similarly, a strong anisotropy appears in the r.m.s. velocity components, with a strengthening of the horizontal components (see figure 25*b*). Note that this does not change the vertical velocity component since the total energy is larger than in the non-rotating case. On this plot are presented the vertical component u_1 mean profile (also denoted u_v), and the horizontal one $u_h = (u_2 + u_3)/2$ for runs SR, R20 and R3.

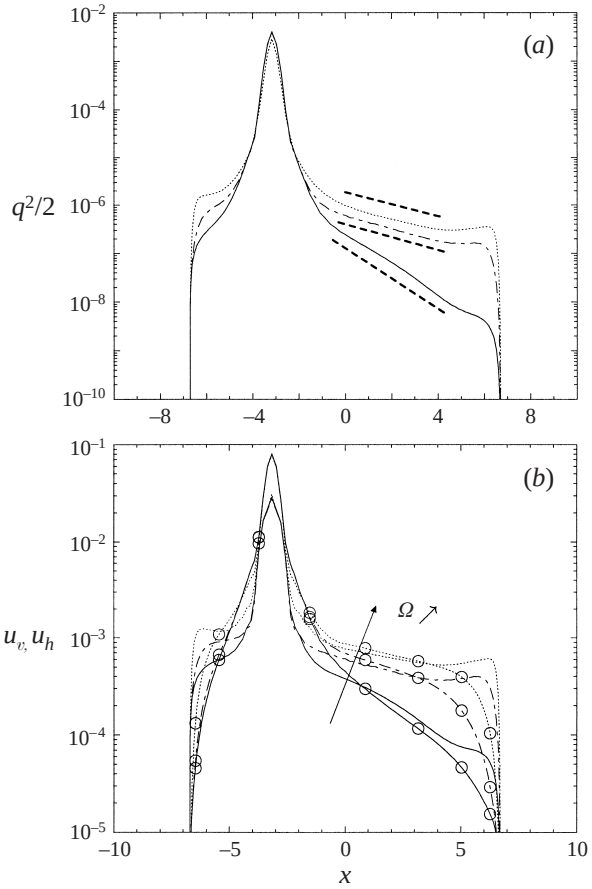

FIGURE 25. Mean profile of (*a*) kinetic energy for: ——, run SR; · — ·, run R20; · · · ·, run R3. (*b*) r.m.s. values of horizontal u_h and vertical velocity components u_v denoted by ○, with the same labels for the different runs.

Run R50 has a higher Reynolds, so that the stationary energy profile is significantly higher than on the three previous runs.

Integral length scales

The evolution of the integral length scales for the three runs is shown on figure 26. It appears that the length scales with vertical separation have the expected behaviour – referring to trends transposed from the homogeneous cases – since the correlation in the vertical direction is larger at high rotation rate. The length with horizontal separation evolves globally as expected, that is it decreases when the rotation rate increases, hence showing the horizontal concentration of vortices. In run R50, we should have expected this length to be larger than in run R20, the latter corresponding to a smaller rotation rate, therefore to fewer structures of larger size (see § 6.6.1). However, $L_{h,v}$ rather seems to be of the same order as that in the high rotation rate case R3. This is not necessarily a proof that vortices in these simulations have similar sizes for we have to remember that the integral length scales are computed by averaging over horizontal planes. In run R3, there are many structures, and this

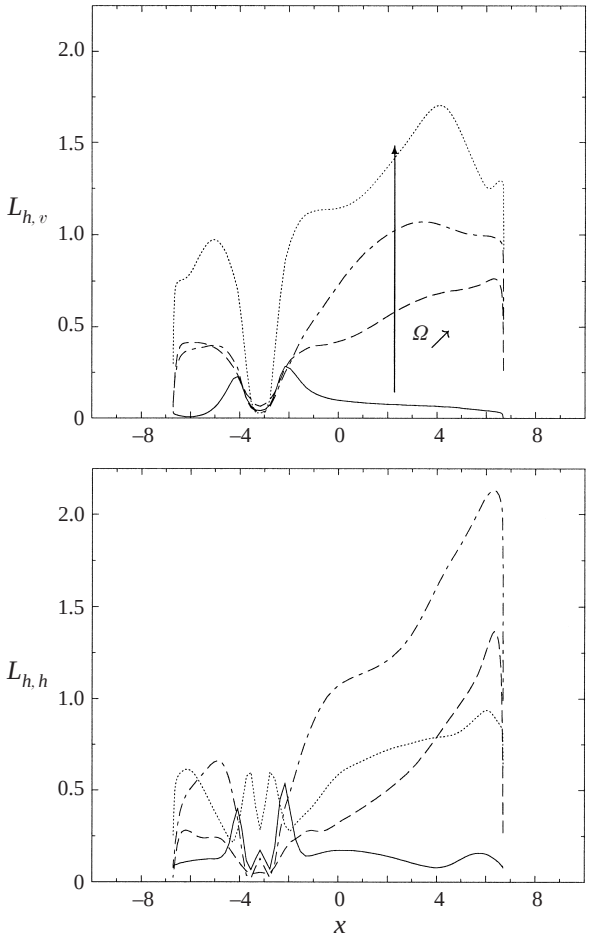

FIGURE 26. Mean profiles of the integral length scales $L_{h,v}$ and $L_{h,h}$ for: ——, run SR; — —, run R50; · — ·, run R20; · · · ·, run R3.

scale is a good estimate for their size. In run R50, only one isolated vortex remains in the box, and such an averaging is no longer valid. This is important since it shows that one has to be careful when trying to relate the length scales and the size of eddies, in relation with intermittency, an important feature of two-dimensional flows. In particular, visualizations are valuable in evaluating the degree of homogeneity of the considered field.

One-dimensional spectra

Figure 27 shows the one-dimensional energy spectra at three locations above the grid ($x' = 3.35,\ 5.90$ and 8.70). We of course find that the energy is larger at larger rotation rate, and decays away from the grid. Moreover, it appears that the spectrum changes gradually when moving away from the grid, with smaller scales affected when the distance increases. Above mode 8, which corresponds to the forcing, energy seems to behave independently from the rotation rate, a clue that rotation is inefficient in modifying the small scales.

In his study of homogeneous statistically steady turbulence, Hossain (1994) has

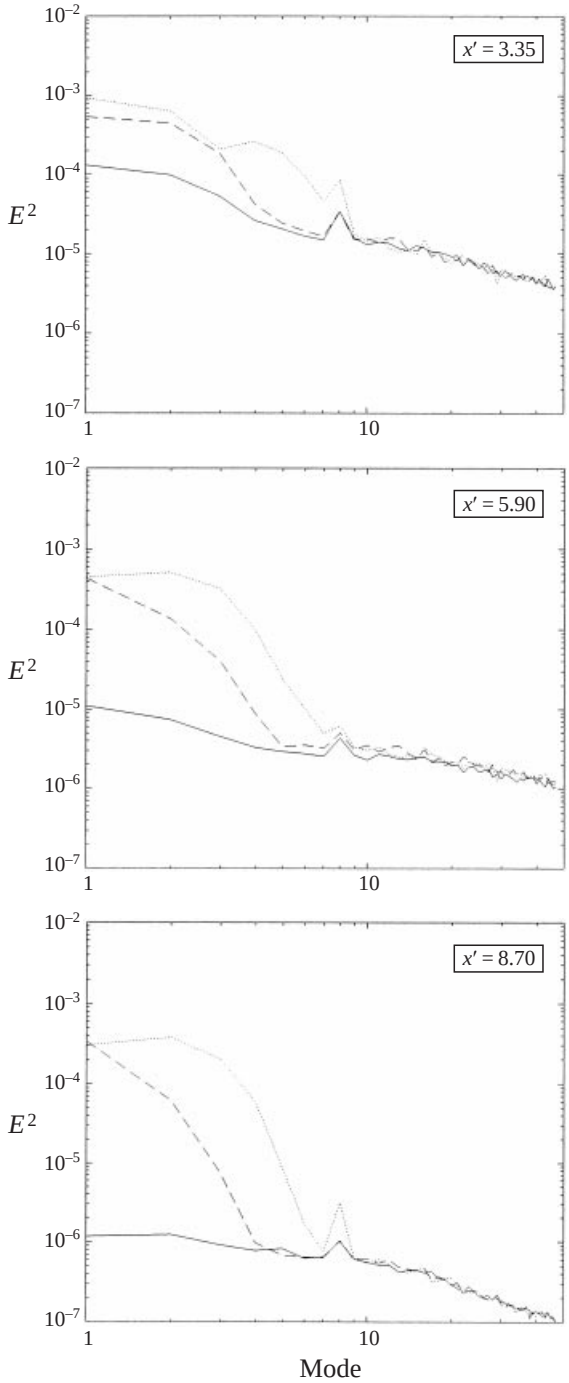

FIGURE 27. One-dimensional spectra of energy at different locations above the grid. —, SR; – –, R20 ; · · · ·, R3. The abcissa is the horizontal wavemode, i.e. the horizontal component of the wavevector non-dimensionalized by the minimum one.

presented three-dimensional energy spectra whose slope at wavenumbers larger than the forcing one depends on the presence of rotation: the $-\frac{5}{3}$ slope without rotation, but a higher -3 one when strong rotation is applied. Comparing these spectral results and ours therefore shows that the small scales of turbulence do not react to rotation in the same way in either homogeneous or diffusive confined flows.

On the contrary, figure 27 demonstrates that the spectra are largely affected by rotation in the large-scale region between modes 1 and 5. We more specifically detect here the decrease of the energy transfer, since, in the rotating case, these modes remain highly energetic with respect to the non rotating-one. Note that a strong trace of the forcing at mode 8 is still present in spectra away from the grid, in the largest rotation rate case.

Transitional Rossby number

In chronological order, we first performed simulation R3, then R20, and finally R50. Runs R3 and R20 have the same resolution which could not give a definite conclusion about whether the transitional Rossby number value given by HBG was retrieved. Since the Reynolds number is the same in the two runs, and the rotation rate decreases from R3 to R20, the latter has produced structures that are limited by the size of the computational domain, and lead to too low Rossby numbers of order 10^{-2}–10^{-3}. A simulation on CRAY T3E of IDRIS allowed us to increase the resolution and the Reynolds number, while keeping the rotation rate low enough. In this run, as we shall see in the visualizations, an isolated cyclone appears when the local Rossby number is in the range 0.2–0.3, which corresponds to the value given by HBG (1982). Yang (1992) has looked for the transitional Rossby number using a different criterion: he locates the minimum of the time-scale inverse $u_h/L_{h,h}$, before it starts increasing again. This argument of minimum, rather than plateau, contradicts the monotonic decrease of the Rossby number with the distance to the grid, and we instead use an 'objective' visualization of the velocity field in planes orthogonal to the rotation axis. The cyclone is well formed starting from the plane at $x' \approx 6.5$–7.0, precisely the region where $Ro^l \sim 0.2$–0.3.

Role of inertial waves and walls in the structuring of the flow

We follow here the analysis by Jacquin (1987) in order to estimate the relative importance of the inertial waves and of confinement in the evolution of turbulence. Three characteristic time scales can be identified:

(a) the decay time scale of homogeneous turbulence $\tau = L/u$, L being an integral length scale ($L \approx 1$) and the amplitude u of fluctuating velocity ($u \approx 0.1$);

(b) the time inertial waves take to propagate over the dimension of the tank, $\tau_t = D/c_g$, where D is the size (between the forcing plane and the upper wall, making it $D \approx 10$) and $c_g = 2\Omega M/(2\pi)$, M being the grid mesh size;

(c) the characteristic time associated with dissipation in the Ekman layer $\tau_p = D/\sqrt{2\Omega\nu}$.

By comparing these time scales, it is thus possible to get a clear picture of the relative importance of the different mechanisms at play. As done by Jacquin, we compare the ratios $I = \tau_t/\tau$ and $J = \tau_p/\tau$, for the three rotating simulations. A low value of I indicates a predominance of the inertial waves in the flow, while a low value of J shows an acceleration of the turbulence decay rate, with respect to the homogeneous case, due to extra dissipation in the Ekman layer. The values obtained are gathered in

Run	2Ω	τ	τ_t	τ_p	$cI = \tau_t/\tau$	$J = \tau_p/\tau$
R3	0.3	100	200	600	2	6
R20	0.05	100	1200	1500	12	15
R50	0.02	50	3000	2300	60	46

TABLE 6. Characteristic time scales for the different mechanisms: τ for the homogeneous decay, τ_t for the propagation of the inertial waves, and τ_p for the wall effects.

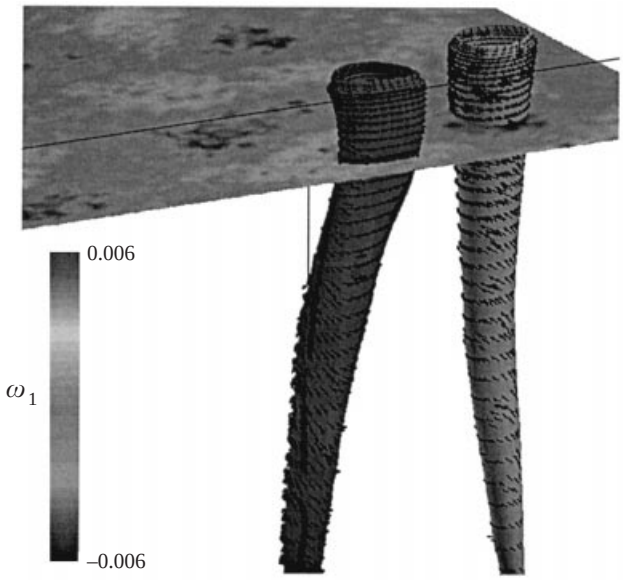

FIGURE 28. Close-up view of two structures identified using the NAM criterion, in run R3, close to the upper wall. One is cyclonic associated with descending motion, the other one is anti-cyclonic with ascending motion, illustrating the Ekman pumping. Vertical vorticity iso-surfaces are shown in a horizontal plane at $x = 5.3$.

table 6. It confirms that inertial waves and wall effects influence the flow more when the rotation rate is large.

6.6.3. *Vortex identification*

Visualizations are added to our previous statistical study, in order to complement the conclusions we have drawn. In the previous § 5, vorticity fields were smooth enough to allow direct use of a vorticity criterion in order to visualize the vortex structures in the flow. It is no longer the case here, due to the strong inhomogeneity of the vorticity field, and to the random component from the forcing, that introduce too much perturbation and noise. We make use of a criterion called NAM (normalized angular momentum), that has been shown by Michard *et al.* (1997) to be useful in the post-processing of experimental and numerical data. Two vortices, anti-cyclonic and cyclonic, are materialized in this way on figure 28, as well as the corresponding velocity field. It can be observed that their identification by the NAM criterion is in agreement with the location of strong vorticity, also represented in a plane on figure 28. It is interesting to observe, using the velocity field also represented, that helical motion is present within these vortices, either in the up or down directions.

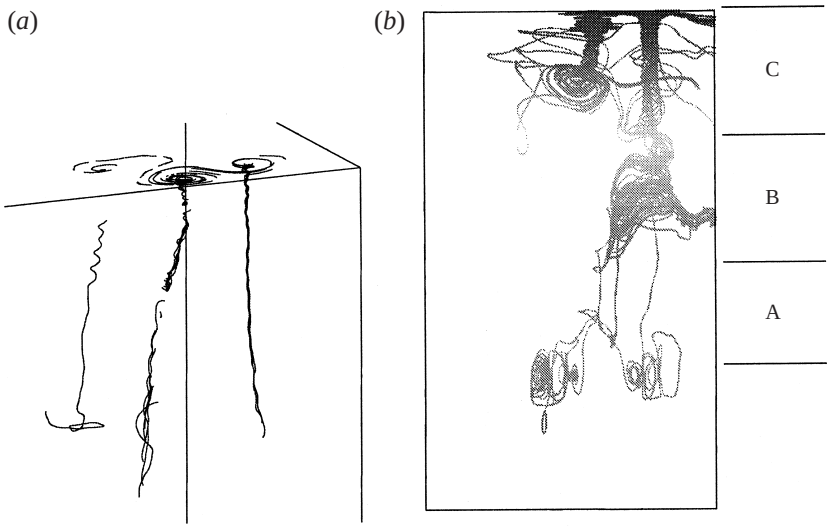

FIGURE 29. (*a*) Materialization of three vortices by particle paths computed in the instantaneous velocity field. The central vortex is cyclonic. (*b*) Regions of the flow identified by the behaviour of particle paths for run R3 (the view is projected onto a vertical plane).

This motion is due to the Ekman pumping phenomenon, but the characteristic step of the helix, away from the wall is $\delta_H \simeq 1$, an order of magnitude larger than the Ekman layer thickness $\delta_E \simeq 0.1$. Of course, very close to the boundary, we recover the fact that $\delta_H \simeq \delta_E$, in agreement with the Ekman pumping mechanism. Additional information on the structuring of the flow can be drawn from the visualization of 'streamlines' described hereafter.

Streamlines for run R3

Although the paths we compute are not exactly fluid particle trajectories, since the flow is unsteady, they exhibit interesting features, worth noting. First, figure 29(*a*) shows the paths obtained by injection of the particles at the axis of the central vortex. We see here that Ekman pumping is already present in the flow, for the central vortex is cyclonic and associated with upward motion. On this figure, vortices extend over half of the wall-to-wall distance. Figure 29(*b*) contains evidence of three distinct regions, wherein the paths are quite different. We first identify region A close to the grid, where the path seem to whirl around the forcing plane. Higher in the tank, the motion becomes more vertically oriented, with a first effect of the rotation appearing (region B). Finally, the last region C, extends up to the upper wall, and shows the predominant effect of rotation with the appearance of vortex structures with axes almost vertical. However, as already mentioned, the transition between zones A and B for this run does not correspond to the transitional Rossby number in the HBG experiment.

6.6.4. *On the existence of intense cyclonic vortices*

In the experiment by HBG, larger values of vorticity are associated with cyclonic vortices. Here, figure 30 shows that the population of cyclones and anti-cyclones is equivalent. It appears that the cyclones are not more intense than anti-cyclones,

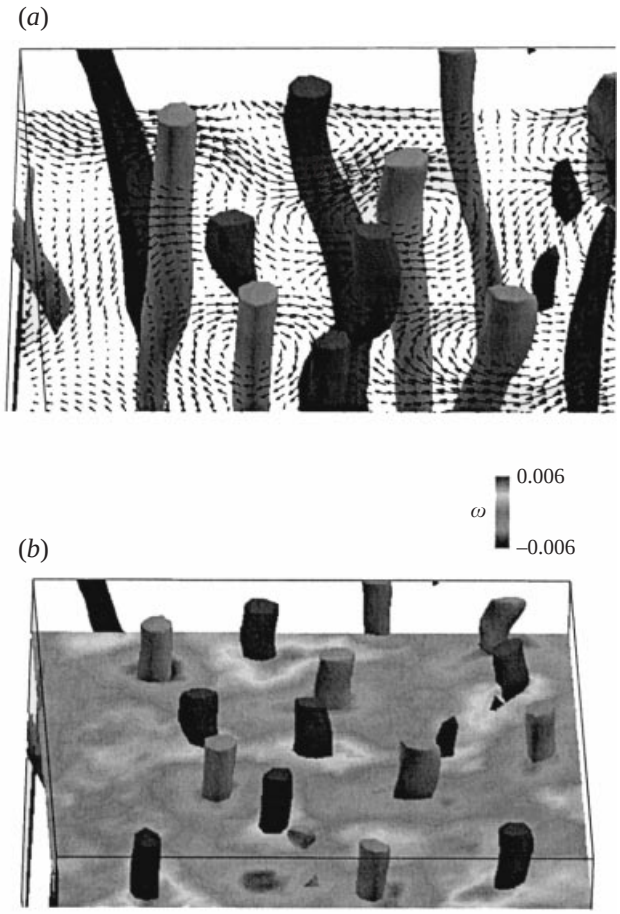

FIGURE 30. For run R3: (*a*) plot of the velocity field in a horizontal plane, and of the three-dimensional structures identified with the NAM criterion; (*b*) iso-lines of vertical vorticity and three-dimensional structures identified by the NAM criterion.

at least in runs R3 and R20, a fact for which we shall now attempt to give an interpretation.

There are certainly two important parameters (probably related in fact): the lifetime of the apparent structures and the corresponding local Rossby number (as the ratio of the characteristic vorticity of the structures to the rotation rate). Let W be the characteristic vorticity of a vortex and the associated characteristic time scale $\tau = 1/W$ (meaning the time necessary for the vortex to rotate once around its axis). The lifetime of the structures can be roughly estimated, in numerical experiments, by following in time the evolution of the velocity field in a plane close to the upper wall ($x = 5.3$). This time d is non-dimensionalized by τ so that it represents the number of turnover times the vortex can undergo before disappearing. Our various observations and quantities have been reported in table 7.

It appears that the vorticity level is lower in runs R3 and R20 that are performed at low Reynolds number, than in run R50 (where vorticity is strongest). It is interesting to note that the lifetime of vortices obtained in run R3 is really small, therefore the structures cannot exactly be qualified as 'persistent'. Without this information on the

Run	W	$Ro^W = W/2\Omega$	d	Identified structures
R3	5×10^{-3}	± 0.015	$\leqslant 1$	Many; as many cyclones as anti-cyclones
R20	5×10^{-3}	± 0.1	≈ 1	Larger, less numerous
R50	0.02	$+1$	$\geqslant 3$	An isolated cyclone

TABLE 7. Recap of the observations on the structuring of the flow in the different computations for the rotating case.

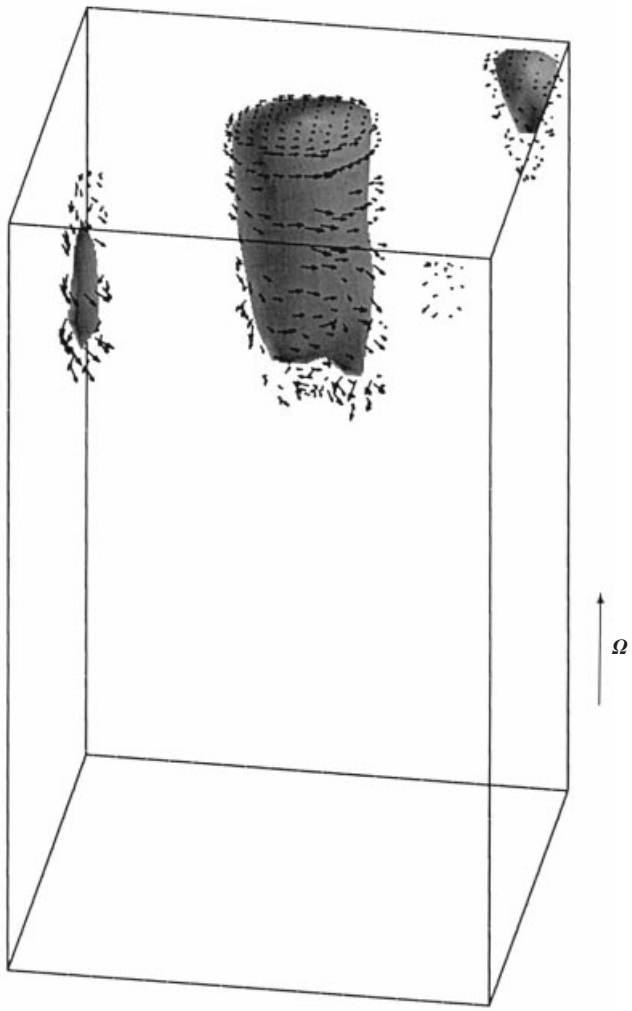

FIGURE 31. Isolated cyclonic vortex obtained in run R50. The entire computational domain between the two solid boundaries is outlined, in order to show the vertical extent of the coherent structure.

life duration of the structures, the weak value of the local Rossby number, in view of linear stability analyses, would have brought us to conclude wrongly that all the vortices are stable. In run R20, the lifetime of vortices is a bit larger, with larger vortices size.

In run R50, the Reynolds number being larger, the vorticity level is higher and the local Rossby number is also larger ($Ro^W = 1$). It seems here that we recover results from linear stability analyses, mentioned in § 2.3, since these predict unstable *anti-cyclones* if $Ro^W \approx -1$. There is indeed, in this run, evidence of only one cyclonic vortex, shown on figure 31. Let us also note that the duration of this structure is quite large ($d > 3$).

Finally, it appears that the domination of cyclonic vortices can exist only if the Reynolds number is large enough, so that vortices can evolve quite independently on a longer time range. A weak value of the Reynolds number seems to lead to a viscous effect that links any cyclonic vortex to an anti-cyclonic one (much like mechanical gears). In that case these pairs are quite short-lived.

7. Conclusion

This work has dealt with a numerical approach to rotating turbulence in a context more complex than homogeneous turbulence. Generally speaking, our study shows that rotation affects turbulence much more than in the simple homogeneous case, when it is associated with other phenomena. Three kinds of simulations have shown the main physical phenomena related to the evolution of confined rotating turbulent flow. Namely, we have simulated the linear regime where inertial waves are clearly observed, and we have identified separately the action of walls, in simulations of freely decaying turbulence, and that of a localized forcing as in the experiment by Hopfinger *et al.* (1982).

In the last case, we have chosen to perform a forcing which is as physical as possible, i.e. which reproduces closely the effects of an oscillating grid. Our simulations have shown that it is quite difficult to generate thick three-dimensional turbulent layers, in which the Reynolds number does not decrease too fast. The closeness of the numerical to experimental forcing has been obtained at the expense of low Reynolds numbers, mainly due to the frequency of the grid and of the rotation parameter whose combination imposes a severe numerical constraint.

Results of freely decaying turbulence simulations show that the walls and rotation influence the energetics parameters and the structure of the flow. Concerning the non-rotating case, results show first that the integral length scale with vertical separation $L_{h,v}$ is affected by the walls from the very beginning of the inhomogeneous case. Its growth is slowed, showing a decrease of the correlation in the vertical direction with respect to the homogeneous case. Second, the length scales tend to get blocked from $t/\tau(0) = 20$ in the homogeneous case, due to the size of the periodic box, whereas the limitation of these scales in the inhomogeneous simulation have a physical explanation which is the confinement of the turbulence structures. We observe the peculiar behaviour of the skewness of derivatives of vertical and horizontal velocity components. The fact that S_v is larger than S_h is in agreement with the physical interpretation of the skewness: vortex stretching is weaker in the direction normal to the walls. Considering the rotating cases, we note that the decrease of total kinetic energy does not vary much from one run to the other, with the same ratio to the non-rotating case. Although rotation is known to reduce the temporal decrease rate of energy by reduction of the energy transfer, it is nonetheless a nonlinear phenomenon,

when the Rossby number Ro^v is close to unity, provided the Reynolds number is large enough. In the presented cases, the latter is quite low (≈ 18), due to limited computer power, when the Rossby number crosses the critical value, so that linear effects of rotation remain relatively important. In the rotating and non-rotating inhomogeneous cases, the length scales with vertical separation grow, indicating an increase in the correlations in the direction parallel to the rotation axis. The length scales with horizontal separation decrease in agreement with the concentration of the vortices. The Reynolds stress tensor anisotropy, seen from the evolution of b_{11}, is larger in the rotating case than in the non-rotating case. Rotation creates, with the interaction of the walls, a vertical component which is damped at the walls in the absence of rotation. We retrieve the critical Rossby number $Ro^v = 1$ usually found in studies of homogeneous turbulence, but this value may change if the confinement effect on the flow increases. The Ekman number based on the wall-to-wall distance is certainly an important parameter on which depend the evolution of the statistical quantities.

From the above observations, in the forced case that leads to a stationary flow one can expect similar mechanisms as in homogeneous rotating turbulence, by analogy of the time decay of the latter to the spatial decay of forced turbulence away from the grid. In the confined case with forcing, rotation reduces the energy transfer as well, while it does not affect the small scales of the flow. The spatial decrease of energy depends on the rotation rate, and in all cases (rotating or not) follows an exponential law. This phenomenon is linked to the blocking of the integral length scales by the confinement effect, as observed experimentally by Risso (1994). In the rotating cases, these scales, in accordance with the corresponding visualizations, show an increase of the correlation in the direction of the axis of rotation when the rotation rate increases. In parallel, the length scales with horizontal separation are reduced, also in accordance with the concentration of vortices. The structure of the flow tends to a quasi-two-dimensional state when the rotation rate increases. Moreover, the rotating simulations have led us to conclude that the number of vortices is linked to the ratio Re/Ro, which is the inverse of the Ekman number; this statement has appeared important in choosing the simulations parameters, such as the rotation rate and the resolution. This has also permitted us to retrieve the transitional Rossby number given by HBG (0.2–0.3), by using a larger Reynolds and Rossby number simulation. The latter run has also shown that the lifetime of the coherent vortical structures is larger when the Reynolds number is raised. In addition, when this condition is fulfilled, the evolution and stability of the observed structures is in agreement with results of linear stability analyses for isolated vortices, since cyclonic vortices are stable and appear to be long-lived, whereas anti-cyclones disappear, due to the instability to perturbations induced by the surrounding flow. Finally, the inertial waves and the walls influence the flow more or less depending on the runs; this influence is largest when the rotation rate is also largest. It appears that Ekman pumping is a very active phenomenon for the structuring of the flow, with a trace of this effect appearing down to the forcing plane.

From a more global viewpoint, the analysis of the analogy between transition processes in rotating homogeneous turbulence and rotating diffusive turbulence between walls, has to be taken carefully. In homogeneous turbulence, the transition from a three-dimensional to a two-dimensional state is triggered by nonlinearities at high Reynolds number. No such transition may appear from purely linear mechanisms. During the time decay of initially isotropic homogeneous turbulence subjected to rotation, the transition appears on a somewhat 'slow' basis. In our case of rotating forced turbulence, the transition happens 'abruptly' in space, from an almost isotropic

homogeneous turbulent region, close to the grid, to a strongly structured region that extends up to the walls. This was also observed in the experiment by HBG. In this respect, our simulations agree quite well with theirs, even considering the critical value of the Rossby number. The experiment was however performed at higher Reynolds number, so that the structuring and transition are due to combined nonlinear and linear effects. Our lower Reynolds number simulation contains mostly the linear effects of rotation and confinement, namely inertial waves and Ekman pumping. Results compare nonetheless well with the experiment, so that it may be concluded that even weak nonlinearities, coupled to the strong effect of confinement, affect strongly the structure of rotating turbulence.

The authors thank Dr Cambon for many fruitful discussions. The homogeneous isotropic spectral code was provided by Professor Staquet. Calculations have been partly performed on the Cray T3E of IDRIS (CNRS computer center), thanks to computing time allocated by the Scientific Council of IDRIS.

REFERENCES

Bardina, J., Ferziger, J. M. & Rogallo, R. S. 1985 Effect of rotation on isotropic turbulence: computation and modelling. *J. Fluid Mech.* **154**, 321–336.

Bartello, P., Métais, O. & Lesieur, M. 1994 Coherent structures in rotating three-dimensional turbulence. *J. Fluid Mech.* **273**, 1–29.

Batchelor, G. K. 1953 *The Theory of Homogeneous Turbulence*. Cambridge University Press.

Bouvard, M. & Dumas, H. 1967 Application de la méthode du fil chaud à la mesure de la turbulence dans l'eau. *Houille Blanche* **22**, 723–733.

Bradshaw, P. 1969 The analogy between streamline curvature and buoyancy in turbulent shear flow. *J. Fluid Mech.* **36**, 177–191.

Briggs, D. A., Ferziger, J. H., Koseff, J. R. & Monismith, S. G. 1996 Entrainment in a shear-free turbulent mixing layer. *J. Fluid Mech.* **310**, 215–242.

Cambon, C., Benoît, J.-P., Shao, L. & Jacquin, L. 1994 Stability analysis and large-eddy simulation of rotating turbulence with organized eddies. *J. Fluid Mech.* **278**, 175–200.

Cambon, C., Mansour, N. N. & Godeferd, F. S. 1997 Energy transfer in rotating turbulence. *J. Fluid Mech.* **337**, 303–332.

Canuto, C., Hussaini, M. Y., Quarteroni, A. & Zang, T. A. 1988 *Spectral Methods in Fluid Dynamics*. Springer.

Carnevale, G. F., Briscolini, M., Kloosterziel, R. C. & Vallis, G. K. 1997 Three-dimensionally perturbed vortex tubes in a rotating flow. *J. Fluid Mech.* **341**, 127–163.

Colin de Verdières, A. 1980 Quasi-geostrophic turbulence in a rotating homogeneous fluid. *Geophys. Astrophys. Fluid Dyn.* **15**, 213–251.

Craik, A. D. D. 1989 The stability of unbounded two- and three-dimensional flows subjected to body forces: some exact solutions. *J. Fluid Mech.* **198**, 275–292.

Dang, K. & Roy, Ph. 1985 Direct and large eddy simulations of homogeneous turbulence submitted to solid body rotation. In *Turbulent Shear Flows 5*. Springer.

De Silva, I. P. D. & Fernando, H. J. S. 1994 Oscillating grids as a source of nearly isotropic turbulence. *Phys. Fluids* **6**, 2455–2464.

Drayton, M. J. 1993 Eulerian and Lagrangian study of inhomogeneous turbulence generated by an oscillating grid. PhD thesis, University of Cambridge.

Greenspan, H. P. 1968 *The Theory of Rotating Fluids*. Cambridge University Press (republished by Breulelen Press, Brookline).

Heikes, K. E. & Maxworthy, T. 1982 Observations of inertial waves in a homogeneous rotating fluid. *J. Fluid Mech.* **125**, 319–345.

Hopfinger, E. J., Browand, F. K. & Gagne, Y. 1982 Turbulence and waves in a rotating tank. *J. Fluid Mech.* **125**, 505–534 (referred to herein as HBG).

Hopfinger, E. J. & Heijst, G. J. F. van 1993 Vortices in rotating fluids. *Ann. Rev. Fluid Mech.* **25**, 241.

Hopfinger, E. J. & Toly, J. A. 1976 Spatially decaying turbulence and its relation to mixing across density interfaces. *J. Fluid Mech.* **78**, 155–175.

Hossain, M. 1994 Reduction in the dimensionality of turbulence due to a strong rotation. *Phys. Fluids* **6**, 1077–1080.

Hossain, M. 1996 Inverse cascades in incompressible fluid and magnetofluid turbulence. *J. Plasma Phys.* **56**, 467.

Ibbetson, A. & Tritton, D. J. 1975 Experiments in turbulence in a rotating fluid. *J. Fluid Mech.* **68**, 639–672.

Jacquin, L. 1987 Étude théorique et expérimentale de la turbulence homogène en rotation. Thèse de Doctorat d'Etat, ONERA.

Jacquin, L., Leuchter, O., Cambon, C. & Mathieu, J. 1990 Homogeneous turbulence in the presence of rotation. *J. Fluid Mech.* **220**, 1–52.

Johnston, J. P., Halleen, R. M. & Lezius, D. K. 1972 Effects of spanwise rotation on the structure of two-dimensional fully developped channel flow. *J. Fluid Mech.* **56**, 533–557.

Kim, J. & Moin, P. 1985 Application of a fractional-step method to incompressible Navier-Stokes equations. *J. Comput. Phys.* **59**, 308–323.

Kloosterziel, R. C. 1990 Barotropic vortices in a rotating fluid. PhD thesis, University of Utrecht, The Netherlands.

Kristoffersen, R. & Andersson, H. I. 1993 Direct simulations of low-Reynolds-number turbulent flow in a rotating channel. *J. Fluid Mech.* **256**, 163–197.

Leblanc, S. 1997 Instabilités tridimensionnelles dans un fluide en rotation. Thèse de Doctorat, Ecole Centrale de Lyons.

Leblanc, S. & Cambon, C. 1997 On the three-dimensional instabilities of plane flows subjected to Coriolis force. *Phys. Fluids* **9**, 1307–1316.

Long, R. R. 1978 Theory of turbulence in an inhomogeneous fluid induced by an oscillating grid. *Phys. Fluids* **21**, 1887–1888.

McDougall, T. J. 1979 Measurements of turbulence in a zero-mean-shear mixed layer. *J. Fluid Mech.* **94**, 409–431.

McEwan, A. D. 1970 Inertial oscillations in a rotating fluid cylinder. *J. Fluid Mech.* **40**, 603–639.

Michard, M., Graftieaux, L., Lollini, L. & Grosjean, N. 1997 Identification of vortical structures by a non-local criterion: Applications to P.I.V. measurements ans D.N.S results of turbulent rotating flows. *Proc. Eleventh Symp. on Turbulent Shear Flows, Grenoble.*

Moser, R. D., Moin, P. & Leonard, A. 1983 A spectral numerical method for the Navier-Stokes equations with application to Taylor-Couette flow. *J. Comput. Phys.* **52**, 524–544.

Mowbray, D. E. & Rarity, B. S. H. 1967 A theoretical and experimental investigation of the phase configuration of internal waves of small amplitude in a density stratified liquid. *J. Fluid Mech.* **28**, 1–16.

Orszag, S. A. & Patterson, G. S. 1972 Numerical simulation of three-dimensional homogeneous isotropic turbulence. *Phys. Rev. Lett.* **28**, 76–79.

Pascal, H. & Buffat, M. 1996 L.E.S. of turbulent flows compressed and/or sheared between two walls on parallel computer using a 'Divergence-free' spectral Galerkin method. In *Computational Fluid Dynamics*, pp. 884–891. Wiley & Sons.

Pasquarelli, F., Quateroni, A. & Sacchi-Landriani, G. 1987 Spectral approximations of the Stokes problem by divergence-free functions. *J. Sci. Comput.* **2**, 195–226.

Pedley, T. J. 1969 On the stability of viscous flow in a rapidly rotating pipe. *J. Fluid Mech.* **128**, 97–115.

Pedloski, J. 1986 *Geophysical Fluid Dynamics*, 2nd Edn. Springer.

Phillips, O. M. 1963 Energy transfer in rotating fluids by reflection of inertial waves. *Phys. Fluids* **6**, 513–520.

Risso, F. 1994 Déformation et rupture d'une bulle dans une turbulence diffusive. Thèse, I.N.P. Toulouse, Institut de Mécanique des Fluides de Toulouse.

Rogallo, R. S. 1981 Numerical experiments in homogeneous turbulence. *NASA Tech. Mem.* 81315.

Tavoularis, S., Bennet, J. C. & Corrsin, S. 1978 Velocity-derivative skewness in small Reynolds number, nearly isotropic turbulence. *J. Fluid Mech.* **88**, 63–69.

Taylor, G. I. 1921 Experiments with rotating fluids. *Proc. Camb. Phil. Soc.* A **100**, 114–121.

Thompson, S. M. & Turner, J. S. 1975 Mixing across an interface due to turbulence generated by an oscillating grid. *J. Fluid Mech.* **67**, 349–368.

Tillmark, N. & Alfredsson, P. H. 1996 Experiments on rotating plane Couette flow. In *Advances in Turbulence VI*. Kluwer.

Veronis, G. 1970 The analogy between rotating and stratified fluids. *Ann. Rev. Fluid Mech.* **2**, 37–66.

Wigeland, R. A. & Nagib, H. M. 1978 Grid generated turbulence with and without rotation about the streamwise direction. *IIT Fluid and Heat Transfer Rep.* R.78-1. Illinois Institute of Technology.

Yang, G. 1992 DNS of boundary forced turbulent flow in a non-rotating and a rotating system. PhD thesis, Cornell University.